https://doi.org/10.5194/egusphere-2026-2606
Preprint. Discussion started: 29 July 2026

Development and evaluation of a crop-specific WRF-VPRM framework: Integrating dynamic phenology and high-resolution distributions for agricultural CO_2 exchange in China

Jiayao Yu[1,5,6], Shuyu Zhao[2], Weiwei Liu[1,5,6], Chong Wei[3], Honghui Xu[4], Lihua Wang[1,5,6], Gang Yang[1,5,6], Weiwei Sun[1,5,6], Tian Feng[1,5,6]*

[1] School of Geography and Remote Sensing, Ningbo University, Ningbo 315211, China
[2] Ningbo Meteorological Bureau, Ningbo 315211, China
[3] Shanghai Carbon Data Research Center, Shanghai Advanced Research Institute, Chinese Academy of Sciences, Shanghai 201210, China
[4] Zhejiang Institute of Meteorological Science, Hangzhou 310008, China
[5] Ningbo Key Laboratory of Remote Sensing and Ecological Security of Coastal Zone, Ningbo University, Ningbo 315211, China
[6] Zhejiang-Germany Joint Laboratory on Remote Sensing of Coastal Ecosystem, Ningbo University, Ningbo 315211, China
Corresponding author: fengtian@nbu.edu.cn

https://doi.org/10.5194/egusphere-2026-2606
Preprint. Discussion started: 29 July 2026

Abstract

Accurate quantification of CO_2 fluxes in China's agricultural ecosystems is frequently hindered by the high spatiotemporal heterogeneity of crop types and phenology, which standard modeling frameworks often oversimplify. This study develops a crop-specific WRF-VPRM framework specifically designed for China's complex agricultural landscape by replacing the generic cropland category with three distinct modules for rice, wheat, and maize. The primary innovation lies in the integration of high-resolution daily crop distribution data and dynamic phenological information, allowing for the optimization of core VPRM parameters to reflect crop-specific photosynthetic pathways and growing seasons. Simulation results for central and eastern China reveal a national gross ecosystem exchange (GEE) and net ecosystem exchange (NEE) of 1084.7 and 779.2 TgC yr^{-1}, respectively, with maize and rice jointly contributing over 80% of total carbon uptake. The model's reliability is underscored by strong correlations between simulated NEE and provincial grain yields, alongside high consistency with OCO-2 satellite XCO_2 retrievals. This refined, online-coupled system provides a more granular perspective on China's agricultural carbon budget and offers a robust modeling tool for evaluating the feedback between crop-specific carbon dynamics and regional climate change.

Keywords: WRF-VPRM; CO_2 flux; rice; wheat; maize; cropland ecosystem

https://doi.org/10.5194/egusphere-2026-2606
Preprint. Discussion started: 29 July 2026

1 Introduction

The exchange of carbon dioxide (CO_2) between the terrestrial biosphere and the atmosphere is a cornerstone of the global carbon cycle, significantly modulating climate variability at both regional and global scales (Entekhabi et al., 1995). Agricultural ecosystems, characterized by intensive carbon assimilation during the growing season, serve as vital net CO_2 sinks and play a strategic role in mitigating the rise of atmospheric greenhouse gas concentrations (Schmidt et al., 2012). As the world's largest grain producer, China's carbon budget is heavily influenced by its dominant cereal crops, i.e., rice, wheat, and maize. During their peak growth stages, these crops drive intense photosynthetic CO_2 drawdown, reshaping regional atmospheric CO_2 gradients (Søgaard et al., 2003). However, quantifying these fluxes remains challenging due to the high spatiotemporal variability of agricultural activities and the short-term fluctuations (hourly to seasonal) in atmospheric transport, which are often poorly captured in current carbon monitoring frameworks (Mauder et al., 2013; Béziat et al., 2009).

Accurate estimation of regional CO_2 fluxes requires bridging the gap between site-level observations and large-scale atmospheric modeling. While eddy covariance (EC) provides high-fidelity local measurements, its sparse network limits its representativeness for complex regional carbon dynamics (Yu et al., 2006). Conversely, atmospheric inversion modeling and process-based ecosystem models offer broader coverage but are often hampered by large uncertainties in transport mechanisms and the difficulty of parameterizing biogeochemical processes across heterogeneous landscapes (Peters et al., 2007; Shi et al., 2018). To address these limitations, coupled atmospheric, biosphere modeling frameworks, such as the Weather Research and Forecasting model integrated with the Vegetation Photosynthesis and Respiration Model (WRF-VPRM), have emerged as powerful tools (Ahmadov et al., 2007). By utilizing satellite-derived indices and meteorological drivers, WRF-VPRM enables the simulation of

https://doi.org/10.5194/egusphere-2026-2606
Preprint. Discussion started: 29 July 2026

high-resolution CO_2 transport and exchange, providing insights into the interactions between mesoscale atmospheric dynamics and biospheric fluxes (Jamroensan et al., 2013).

Despite its widespread application in various regions (Huggannavar et al., 2023; San José et al., 2025), the standard WRF-VPRM framework exhibits a critical deficiency in agricultural CO_2 simulation: it treats cropland as a single, generic vegetation category (Hilton et al., 2013; Park et al., 2018). In reality, the three major crops, rice, wheat, and maize, possess fundamentally different photosynthetic pathways (C3 vs. C4), phenological cycles, and water-use efficiencies (Wang et al., 2023). For instance, the submerged conditions of paddy rice and the high photosynthetic capacity of C4 maize lead to vastly different carbon exchange signatures (Kumar et al., 2021). Applying a uniform parameter set to represent all crop types inevitably leads to systematic biases in regional carbon budgets, particularly in China where these crops are distributed across diverse climatic zones with overlapping growing seasons. More importantly, the standard model fails to account for the unique growing seasons and precise timing of agricultural activities for different crop types. In regions like China, where multiple cropping systems (e.g., wheat-summer maize rotation) are prevalent, the carbon source-to-sink transition is governed by human-defined crop calendars rather than just climate-driven green-up. Without integrating crop-specific daily-scale distribution maps, the coupled model inevitably introduces significant errors in the timing and magnitude of simulated CO_2 pulses, particularly during the rapid transitions of the growing season (Hilton et al., 2013; Park et al., 2018).

To fill these gaps, this study develops a revised WRF-VPRM framework specifically designed for the heterogeneous agricultural landscape of China. The primary innovation lies in the replacement of the generic cropland category with three distinct crop-specific modules for rice, wheat, and maize. By incorporating high-resolution daily crop distribution data and dynamic phenological information, we optimized the four core VPRM parameters (λ, α, β,

https://doi.org/10.5194/egusphere-2026-2606
Preprint. Discussion started: 29 July 2026

and PAR_0) to reflect the unique physiological traits of each crop. This refined, online-coupled system allows for a more accurate representation of the interaction between crop-specific carbon exchange and regional atmospheric CO_2 concentrations. This research provides a more granular perspective on China's agricultural carbon budget and offers a robust modeling tool for evaluating the impact of crop phenology on regional climate change.

2 Materials and Methods

2.1 Revised WRF-VPRM model for crops

The VPRM model is fully online coupled with WRF V3.9.1 (Ahmadov et al., 2007). The coupled atmosphere–biosphere model WRF-VPRM is therefore able to simulate CO_2 exchange between terrestrial ecosystems and the atmosphere over China. In VPRM, NEE is defined as the sum of RESP and GEE (Mahadevan et al., 2008):

$$NEE = GEE + RESP \tag{1}$$

where, RESP represents the combined autotrophic respiration of vegetation and heterotrophic respiration of soil microorganisms. Positive RESP indicates CO_2 release to the atmosphere, while GEE represents CO_2 uptake through photosynthesis and is therefore negative. RESP and GEE are parameterized as:

$$RESP = \alpha \times T + \beta \tag{2}$$

$$GEE = -\lambda \times T_{scale} \times W_{scale} \times P_{scale} \times \frac{1}{1 + \frac{PAR}{PAR_0}} \times FAPAR_{PAV} \times PAR \tag{3}$$

where, RESP depends on air temperature at 2 m (T), where α and β are empirical parameters, and RESP is set to zero when $T < -\beta/\alpha$. GEE depends on maximum light-use efficiency (λ), temperature scaling (T_{scale}), water stress scaling (W_{scale}), phenology scaling (P_{scale}), photosynthetically active radiation (PAR), the half-saturation parameter (PAR_0), and the fraction of absorbed PAR ($FAPAR_{PAV}$). The absorbed PAR fraction is estimated using the

https://doi.org/10.5194/egusphere-2026-2606
Preprint. Discussion started: 29 July 2026

Enhanced Vegetation Index (EVI), which is closely related to photosynthetic activity and canopy structure (Huete et al., 2002; Jiang et al., 2008). Near-surface PAR is derived from downward shortwave radiation (SWDOWN) using the relationship $PAR = SWDOWN/0.505$ (Dayalu et al., 2018). The scaling factors are defined as:

$$T_{scale} = \frac{(T - T_{min})(T - T_{max})}{(T - T_{min})(T - T_{max}) - \left(T - T_{opt}\right)^2} \tag{4}$$

$$W_{scale} = \frac{1 + LSWI}{1 + LSWI_{max}} \tag{5}$$

$$P_{scale} = \frac{1 + LSWI}{2} \tag{6}$$

Here, T_{scale} describes the temperature dependence of photosynthesis and is determined by vegetation-specific parameters including minimum (T_{min}), optimal (T_{opt}), and maximum (T_{max}) temperatures (Xiao et al., 2004). The land surface water index (LSWI) reflects vegetation water content, with $LSWI_{max}$ representing the maximum seasonal value for each grid cell (Chandrasekar et al., 2010). W_{scale} represents water stress effects, while P_{scale} accounts for phenological changes. Evergreen vegetation is assigned a constant value of 1, whereas deciduous and grassland vegetation vary seasonally. Figures 1a–b show the spatial distribution of mean EVI and LSWI in eastern and central China for 2020.

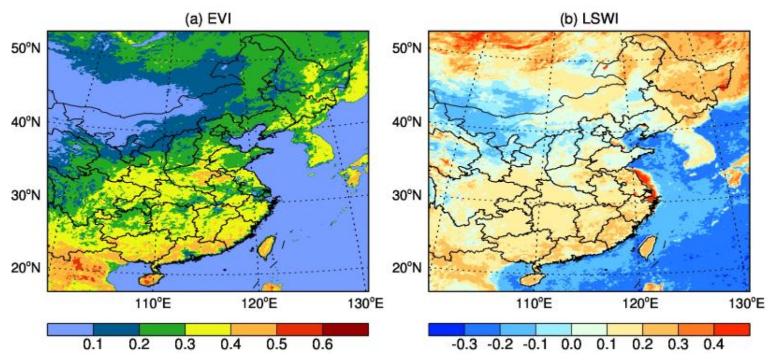

Figure 1. Spatial distribution of the annual mean Enhanced Vegetation Index (EVI) **(a)** and Land Surface Water Index (LSWI) **(b)** in eastern and central China, derived from MODIS MOD09A1 surface reflectance data.

https://doi.org/10.5194/egusphere-2026-2606
Preprint. Discussion started: 29 July 2026

EVI and LSWI were derived using the VPRM preprocessor from the MODIS level-3 surface reflectance product MOD09A1.061, which has a spatial resolution of 500 m and a temporal resolution of 8 days (https://search.earthdata.nasa.gov/search). After atmospheric correction, this dataset provides reliable vegetation and surface information and has been widely used in ecological and climate studies (Vermote et al., 2021; Hill et al., 2020). Vegetation type information is obtained from the SYNMAP global vegetation dataset with a spatial resolution of 1 km (Jung et al., 2006). Vegetation is classified into eight land-cover categories: evergreen forest, deciduous broadleaf forest, mixed forest, shrubland, savanna, cropland, grassland, and urban/water bodies. The VPRM preprocessor integrates SYNMAP and MODIS indices with the WRF grid to generate key vegetation parameters, including EVI, LSWI, vegetation fraction (VEGFRA), and their seasonal extremes (EVI_{max}, EVI_{min}, $LSWI_{max}$, $LSWI_{min}$).

Following Dayalu et al., (2018), we adapted the key VPRM parameters (λ, α, β, and PAR_0) to China's climate and crop characteristics. Specifically, the parameters for rice in Dayalu et al., (2018) are actually the same as those for grass. We updated these parameters according to the in-situ measurements at the Changling vortex flux station (44.60°N, 123.47°E, Figure 1a) using an improved Levenberg–Marquardt nonlinear least squares method (Feng, 2026). The key parameters for rice, wheat, and maize are listed in Table 1.

Table 1. Photosynthesis and respiration calculation parameters of rice, wheat and maize. Units: λ: μmol CO_2 m^{-2} s^{-1} (μmol PAR m^{-2} s^{-1})$^{-1}$; α: μmol CO_2 m^{-2} s^{-1} K^{-1}; β: μmol CO_2 m^{-2} s^{-1}; PAR_0: μmol m^{-2} s^{-1}.

Parameter	Rice	Wheat	Maize
λ	0.2050	0.1570	0.1430
α	0.1320	0.0870	0.0938
β	0.0334	0.00604	1.42
PAR_0	1082	1205	2070

https://doi.org/10.5194/egusphere-2026-2606
Preprint. Discussion started: 29 July 2026

To better represent crop phenology, a national high-resolution phenology dataset for the three major grain crops in China (ChinaCropPhen1km) was incorporated (Luo et al., 2020). This dataset provides detailed information on crop distribution and phenological timing and has been used to simulate seasonal variations in CO_2 flux during key growth stages of rice, wheat, and maize. After removing scattered cropland pixels, the simulated planting areas of rice, wheat, and maize in 2020 were 30.06, 23.34, and 41.32 million hectares, respectively, which are consistent with official statistics reported by the National Bureau of Statistics (30.08, 23.38, and 41.26 million hectares) (https://www.stats.gov.cn/sj/ndsj/2024/indexch.htm). The spatial distributions and daily temporal variations of rice, wheat, and maize are presented in Figures 2 and 3, respectively.

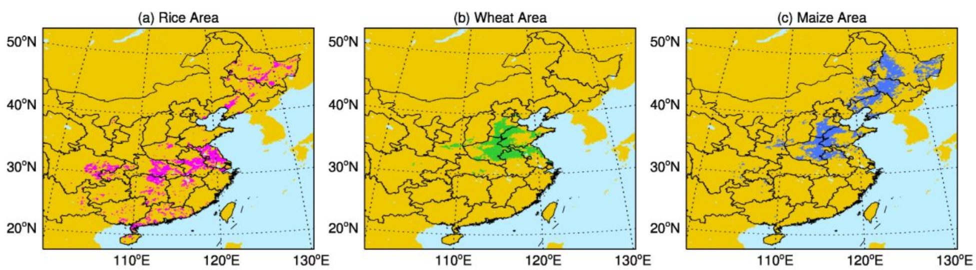

Figure 2. Spatial distribution of simulated cropland areas for rice **(a)**, wheat **(b)**, and maize **(c)** across China based on the ChinaCropPhen1km phenology dataset (Luo et al., 2020).

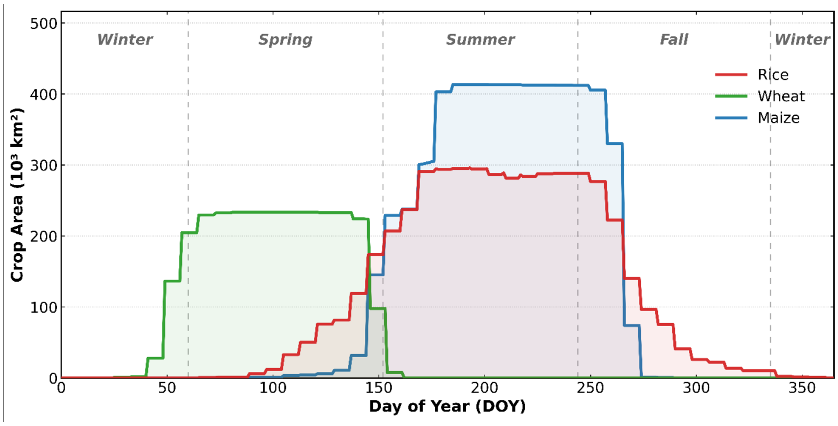

Figure 3. Daily cultivation areas of rice, wheat, and maize in the study domain. Gray dashed lines denote boundaries for each season.

2.2 Model configuration

The simulation domain covers the major planting regions of rice, wheat, and maize in China (Figure 4). The model is used to simulate the spatiotemporal variations of CO_2 flux during the growth periods of these three crops in 2020 and to evaluate their contributions to regional land–atmosphere CO_2 exchange.

https://doi.org/10.5194/egusphere-2026-2606
Preprint. Discussion started: 29 July 2026

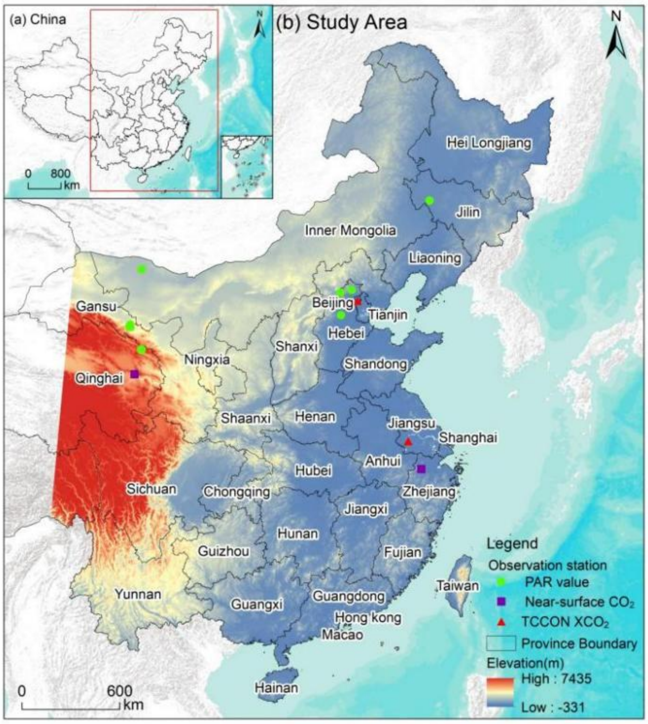

Figure 4. Model simulation domain over eastern and central China **(a)** and detailed map showing elevation (m a.s.l.), provincial boundaries, and observation sites **(b)**. Observation sites include PAR stations (green circles), near-surface CO_2 stations (purple squares), and TCCON stations (red triangles).

The WRF-VPRM model is configured with a single nested domain centered at 116°E, 36.5°N, with a horizontal resolution of 9 km × 9 km and a grid size of 360 × 360. The vertical structure includes 35 stretched layers, with layer thickness increasing from 50 m near the surface to 500 m at 2.5 km and exceeding 1 km above 14 km.Meteorological initial and boundary conditions are derived from the NCEP FNL reanalysis dataset (1° × 1°, 6 h interval). CO_2 initial and boundary conditions are obtained from the Jena CarboScope s10oc_v2023 (https://www.bgc-jena.mpg.de/CarboScope/?ID=s10oc_v2023) dataset at 6 h intervals

https://doi.org/10.5194/egusphere-2026-2606
Preprint. Discussion started: 29 July 2026

(Rödenbeck et al., 2003). Anthropogenic CO_2 emissions are taken from the MEIC emission inventory developed by Tsinghua University with a spatial resolution of 0.25° × 0.25°, including contributions from industry, power generation, residential, and transportation sectors (Li et al., 2017).The main physical parameterization schemes used in the WRF model include the WSM6 microphysics scheme (Cintineo et al., 2014), MYJ planetary boundary layer scheme (Janjić et al., 2002), Monin–Obukhov surface layer scheme (Yee et al., 1998), and the Noah land surface model (Chen et al., 2001). Shortwave and longwave radiation are calculated using the (Dudhia, 1989) and RRTM (Mlawer et al., 1997) schemes, respectively. Cumulus convection and CO_2 dry deposition are represented by the Kain–Fritsch (Kain, 2004) and Wesely (Wesely, 1989) schemes. The full model configuration is summarized in Table 2.

Table 2. Model configuration for the simulation domain, meteorological schemes, initial and boundary conditions, and emission inventories.

Category	Item	Configuration
Basic Model Setup	Period	Jan 01 – Dec 31, 2020
	Region	Eastern and central China
	Domain center	116°E, 36.5°N
	Domain size	3240 km ×4140 km
	Horizontal resolution	9 km × 9 km
	Vertical resolution	35 vertical levels
	Map projection	Lambert conformal conic
Physical Parameterizations	Microphysics scheme	WRF Single-Moment 6-class scheme
	Cumulus parameterization	Kain-Fritsch scheme
	Boundary layer scheme	MYJ TKE scheme
	Surface layer scheme	Monin-Obukhov scheme
	Land-surface scheme	Noah land surface model
	Radiation schemes	Dudhia (shortwave); Mlawer (longwave) scheme
Boundary & Initial Conditions	Meteorological boundary and initial condition	NCEP FNL 1° × 1° analysis data
	Chemical boundary and initial condition	Jena CarboScope 6-h output
CO_2 Flux Inputs	Anthropogenic emission inventory	MEIC emission inventory

https://doi.org/10.5194/egusphere-2026-2606
Preprint. Discussion started: 29 July 2026

	Terrestrial CO_2 fluxes	VPRM output
Simulation Control	Spin-up time	40 hours

2.3 Observations

To evaluate the reliability of the model simulations, multiple observational datasets were used for comparison. PAR observations covering all four seasons were obtained from the Changling (Dong et al., 2022), Gucheng (Zhou et al., 2023), Haibei grassland and Haibei shrubland (Zhang et al., 2023), Heihe Daman, Heihe Remote Sensing, Heihe Mixed Forest, Heihe Zhangye (Xu et al., 2024), Huailai (Xu et al., 2023), and Yanshan shrubland (Du et al., 2023) (Figure. 4). Near-surface CO_2 concentration data were obtained from the Lin'an and Waliguan stations. Column-averaged CO_2 (XCO_2) data were derived from satellite retrievals of the Orbiting Carbon Observatory-2 (OCO-2) (Connor et al., 2008) and combined with ground-based observations from the Total Carbon Column Observing Network (TCCON) (Laughner et al., 2024) at Hefei and Xianghe (Figure. 5). In addition, the simulation results were compared with the CarbonTracker (http://carbontracker.noaa.gov) CT2022 dataset from the National Oceanic and Atmospheric Administration (NOAA) (Jacobson et al., 2023) (Figure. 6).

2.4 Statistics for model-observation comparison

The model performance was evaluated using the mean bias (MB), root mean square error (RMSE), index of agreement (IOA), and correlation coefficient (r). Here, P_i and O_i denote the simulated and observed values at time i, respectively, N is the sample size, and $\bar{O}$ represents the mean observation. The formulas are given as follows:

$$\mathrm{MB} = \frac{1}{\mathrm{N}}\sum_{\mathrm{i}=1}^{\mathrm{N}}(\mathrm{P_i} - \mathrm{O_i}) \tag{7}$$

https://doi.org/10.5194/egusphere-2026-2606
Preprint. Discussion started: 29 July 2026

$$\mathrm{RMSE} = \left[\frac{1}{N}\sum_{i=1}^{N}(P_i - O_i)^2\right]^{\frac{1}{2}} \tag{8}$$

$$\mathrm{IOA} = 1 - \frac{\sum_{i=1}^{N}(P_i - O_i)^2}{\sum_{i=1}^{N}(|P_i - \bar{O}| + |O_i - \bar{O}|)^2} \tag{9}$$

$$r = \frac{\mathrm{cov}(P, O)}{\sigma P\ \sigma O} = \frac{\left(\sum_{i=1}^{N} P_i O_i - \frac{\sum_{i=1}^{N} P_i O_i}{N}\right)}{\sqrt{\left(\sum_{i=1}^{N} P_i^2 - \frac{(\sum_{i=1}^{N} P_i)^2}{N}\right)\left(\sum_{i=1}^{N} O_i^2 - \frac{(\sum_{i=1}^{N} O_i)^2}{N}\right)}} \tag{10}$$

3 Results and Discussion

3.1 Model performance

3.1.1 Photosynthetically active radiation (PAR)

PAR is a key factor controlling photosynthesis and respiration in terrestrial ecosystems and plays an important role in simulating biosphere–atmosphere carbon fluxes (Baldocchi, 2008). Both simulated and observed PAR by the WRF-VPRM model exhibit a typical unimodal diurnal pattern with a peak around 13:00, accompanied by a pronounced seasonal gradient (Figure 5a–d). The observed peak reaches the maximum in summer (1289.38 mmol m^{-2} s^{-1}), followed by spring (1183.93 mmol m^{-2} s^{-1}), fall (986.21 mmol m^{-2} s^{-1}), and winter (767.62 mmol m^{-2} s^{-1}), which is fully consistent with the seasonal variation of solar radiation in the Northern Hemisphere. The simulated results accurately reproduce this seasonal gradient and diurnal morphology: the simulated peak in winter (750.17 mmol m^{-2} s^{-1}) shows the smallest deviation from observations (approximately -2.3%), while a slight overestimation is observed in spring (+7.4%), and minor underestimations occur in summer (-2.3%) and fall (-7.0%), with no systematic extreme bias overall.

Regression analysis further confirms the strong linear consistency between simulated and observed PAR (Figure 5e–h). The correlation coefficients reach 1.00 ($p < 0.001$) for all seasons,

https://doi.org/10.5194/egusphere-2026-2606
Preprint. Discussion started: 29 July 2026

and the fitted slopes are close to unity (1.000 in winter, 1.084 in spring, 1.002 in summer, and 0.952 in fall), with data points tightly distributed around the 1:1 line, indicating excellent performance of the model in simulating the absolute magnitude of PAR. The slightly larger slope in spring and smaller slope in fall correspond to minor overestimation and underestimation of PAR by the model, respectively, but these discrepancies remain within an acceptable range. Overall, the model can accurately capture the diurnal–seasonal variation and absolute magnitude of PAR, providing a reliable physical driver for subsequent simulations of carbon fluxes in agricultural ecosystems.

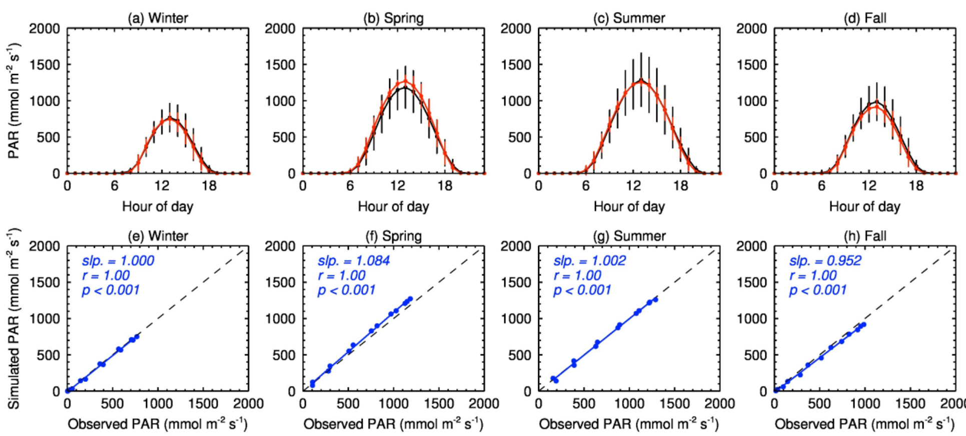

Figure 5. Comparison of observed and simulated PAR across seasons. **(a–d)** Diurnal variations of simulated (red) and observed (black) PAR in winter **(a)**, spring **(b)**, summer **(c)**, and fall **(d)**; shaded areas indicate observational variability. **(e–h)** Scatter plots of observed versus simulated PAR for winter **(e)**, spring **(f)**, summer **(g)**, and fall **(h)**. The dashed line represents the 1:1 line. Slopes and correlation coefficients r are shown for each season, with p-values indicating statistical significance.

3.1.2 Column XCO_2 and near-surface CO_2

https://doi.org/10.5194/egusphere-2026-2606
Preprint. Discussion started: 29 July 2026

(a) Comparisons with in-situ observations and satellite retrievals

The satellite-retrieved dry-air column-averaged CO_2 mole fraction (XCO_2) provides a strong constraint on terrestrial carbon fluxes in global inversion frameworks (Chevallier et al., 2019; Liu et al., 2021). To evaluate model performance in simulating atmospheric CO_2, simulated concentrations were compared with observations of near-surface CO_2 (Figure 6a-b) and column XCO_2 (Figure 6c-e).

The Waliguan global background station is located in a high-altitude region of the Qinghai-Tibet Plateau, characterized by a relatively clean atmospheric background with minimal anthropogenic interference (Figure 6b), where the measurements can reliably reflect changes in atmospheric background CO_2 (Zhou et al., 2005). The model shows slight deviations from the observations at the global background station and the regional background station Lin'an (Figure 6a), with MBs of -0.90 ppm and 1.00 ppm, respectively. Lin'an station is characterized by intensive human activities, complex terrain, and strong underlying surface heterogeneity. The model exhibits a tendency to underestimate when the observations are high. The simulation bias may arise because ground-based observations are more susceptible to factors such as local emission sources and underlying surface heterogeneity, leading to relatively larger simulation errors (Ciais et al., 2014; Thompson et al., 2016). Overall, the model reproduces the CO_2 concentration differences between Waliguan and Lin'an stations reasonably well, with IOAs of 0.80 and 0.66, respectively, indicating that the agreement between model results and observations remains within an acceptable range.

With its high precision and long-term stability, TCCON is widely regarded as the “gold standard” for validating satellite CO_2 retrieval products and model simulations (Morino et al., 2018). At the two TCCON sites, Hefei (Figure 6c) and Xianghe (Figure 5d), the MBs are 0.75 ppm and 0.86 ppm, respectively, with both correlation coefficient (*r*) and IOA exceeding 0.70, indicating that the model performs well in simulating XCO_2 observations. OCO-2 retrieves

https://doi.org/10.5194/egusphere-2026-2606
Preprint. Discussion started: 29 July 2026

XCO_2 by observing reflected solar radiation in three near-infrared bands and employing an optimal estimation algorithm. In terms of the spatial distribution of XCO_2 in the study region, the simulation results also show good consistency with OCO-2 satellite retrievals (Figure 6e), with an IOA as high as 0.91 ($r = 0.84$, $p < 0.001$) and a very small simulation bias of 0.39 ppm. In contrast, the simulation of column-averaged XCO_2 exhibits higher consistency and stability. The XCO_2 in the study region is significantly lower than the near-surface CO_2 concentration at the Lin'an station and is close to the near-surface CO_2 concentration at the Waliguan station. Constrained by posterior flux estimates, modeled XCO_2 biases are generally limited to a range of 0.5–2 ppm (Fu et al., 2019; Xie et al., 2018).

Overall, the model used in this study shows good consistency with observations, suggesting that the model is capable of reliably representing atmospheric CO_2 variations, with notably better performance in simulating column-averaged XCO_2 than near-surface CO_2 concentrations.

https://doi.org/10.5194/egusphere-2026-2606
Preprint. Discussion started: 29 July 2026

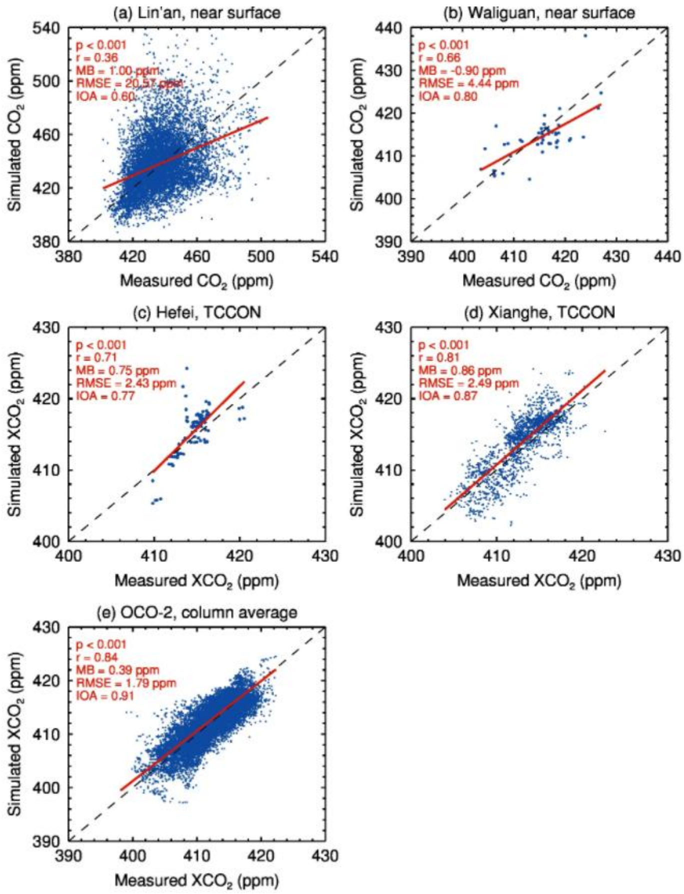

Figure 6. Comparison of simulated and observed CO_2 concentrations at multiple sites. Near-surface CO_2 at Lin'an **(a)** and Waliguan **(b)**; column-averaged XCO_2 at the Hefei **(c)** and Xianghe **(d)** TCCON sites; and OCO-2 satellite-retrieved XCO_2 **(e)**. Red dashed lines indicate linear regression fits between simulated and observed values, and statistical metrics (MB, r, IOA, RMSE) are provided in each panel.

(b) Comparison with CT2022

CarbonTracker integrates global CO_2 observations and model simulations to provide reliable estimates of atmospheric CO_2 fields and is widely used to evaluate regional and global CO_2 simulations (Yuan et al., 2019; Cui et al., 2021). To assess the performance of WRF-

https://doi.org/10.5194/egusphere-2026-2606
Preprint. Discussion started: 29 July 2026

VPRM, its simulated near-surface and column-averaged CO_2 concentrations were compared with CarbonTracker (CT2022) results (Figure 6a–f). The spatial patterns simulated by WRF-VPRM are generally consistent with CT2022 across the study area, particularly showing high concentrations over the North China Plain and the Yangtze River Delta, where the surface CO_2 were above 460 and 440 ppm, XCO_2 were above 414.5 and 415 ppm,respectively. WRF-VPRM captures local emission-related anomalies with finer spatial detail (Figure 7a, d), whereas CT2022 shows smoother distributions in these regions (Figure 7b, e). Our data demonstrate a prominent gradient between industrial and remote areas, especially for surface CO_2. Near-surface CO_2 simulated by WRF-VPRM is generally lower than CT2022 in most areas, with local differences exceeding 15 ppm; however, higher values occur in some high-emission regions of North China, with differences mainly within 15 ppm (Figure 7c). In contrast, biases in column-averaged CO_2 are much smaller, ranging from approximately −2 to 1 ppm (Figure 6f). Overall, both models show small biases in the spatial distribution of surface CO_2 and good overall agreement.

https://doi.org/10.5194/egusphere-2026-2606
Preprint. Discussion started: 29 July 2026

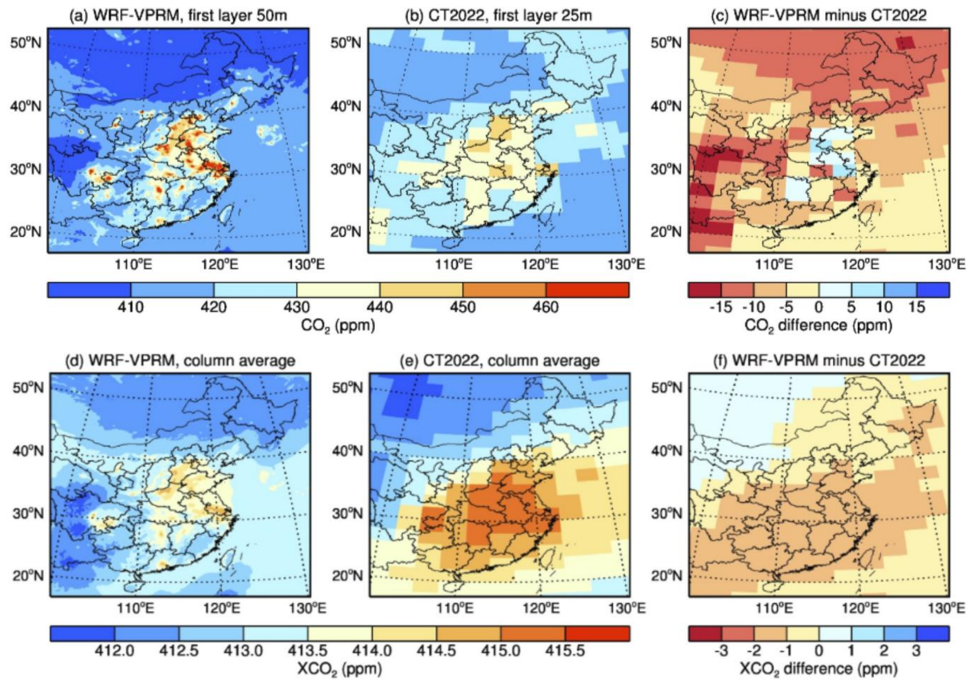

Figure 7. Comparison of near-surface and column-averaged CO_2 concentrations simulated by WRF-VPRM and CarbonTracker (CT2022) over China. Near-surface CO_2 from WRF-VPRM **(a)**, CT2022 **(b)**, and their difference **(c)**; column-averaged CO_2 (XCO_2) from WRF-VPRM **(d)**, CT2022 **(e)**, and their difference **(f)**.

3.2 CO_2 exchanges during crop growth

3.2.1 Spatial patterns

The three major crops exhibit strong net CO_2 uptake during their growth period and represent the main sources of carbon absorption in China's farmland ecosystems. Overall, GEE reaches about 1084.7 $TgC \cdot yr^{-1}$ (Figure 8a), while RESP is 305.5 $TgC \cdot yr^{-1}$ (Figure 8i), resulting in an NEE of 779.2 $TgC \cdot yr^{-1}$ (Figure 8e). CO_2 uptake by these crops greatly exceeds respiratory emissions, highlighting their role in mitigating atmospheric CO_2 increases. Significant differences exist among crop types. For rice, GEE, RESP, and NEE are 429.4, 121.0, and 308.4

https://doi.org/10.5194/egusphere-2026-2606
Preprint. Discussion started: 29 July 2026

$TgC \cdot yr^{-1}$, respectively; for wheat, 173.9, 27.8, and 146.1 $TgC \cdot yr^{-1}$; and for maize, 481.4, 156.7, and 324.7 $TgC \cdot yr^{-1}$, respectively, indicating the highest net uptake for maize. The annual contributions of rice, wheat, and maize to total net CO_2 absorption are 39.6%, 18.8%, and 41.7%, respectively, broadly consistent with the findings of She et al. (2017) that rice accounts for about 48.71% of the total net CO_2 uptake among the three crops. Overall, maize and rice together contribute more than 80% of the total carbon uptake, while wheat, although smaller in magnitude, remains important in certain regions.

In terms of spatial distribution, net CO_2 uptake varies significantly among crop types (Figure 8). RESP generally follows the spatial pattern of GEE, indicating that areas with strong biomass accumulation also exhibit higher respiration. The middle and lower reaches of the Yangtze River, the North China Plain, and the Northeast Plain are the main regions for crop carbon uptake and respiration, playing a key role in the national agricultural carbon cycle. Rice is more widely distributed than wheat and maize, with high CO_2 flux mainly in the middle and lower Yangtze River region and major paddy cultivation areas, especially in the Yangtze–Huaihe basin (Figure 8b, f, j). Wheat fluxes are concentrated in the North China Plain and show relatively lower RESP (Figure 8k). Maize shows strong performance in both Northeast and North China, with high GEE and RESP in the Northeast Plain and correspondingly high NEE, reflecting its strong carbon uptake potential in northern regions (Figure 8d, h, l). The North China region represents the most significant cropland CO_2 sink in China (Li et al., 2006; Han et al., 2020), mainly driven by wheat and maize. In the Northeast, maize dominates net CO_2 uptake and plays a leading role in regional atmospheric CO_2 absorption.

https://doi.org/10.5194/egusphere-2026-2606
Preprint. Discussion started: 29 July 2026

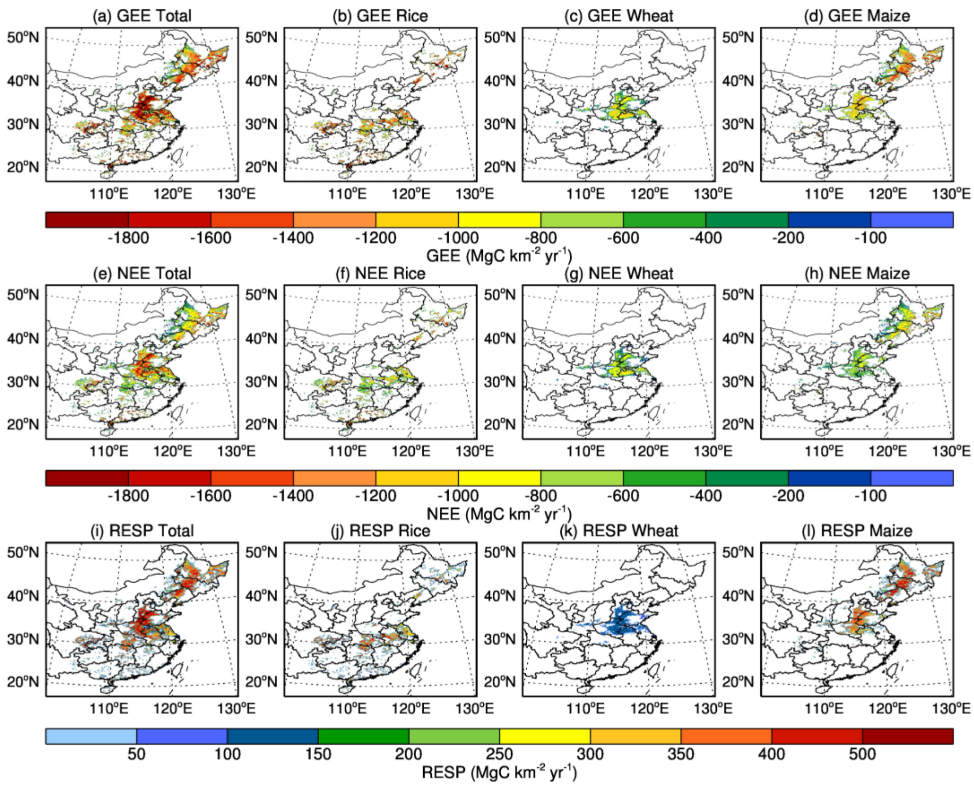

Figure 8. Spatial distribution of crop carbon fluxes (GEE, RESP, and NEE) for major crops in China. Gross ecosystem exchange (GEE) for total crops, rice, wheat, and maize **(a–d)**; net ecosystem exchange (NEE) for the same crops **(e–h)**; and ecosystem respiration (RESP) **(i–l)**. Positive NEE values indicate CO_2 release to the atmosphere, while negative values indicate CO_2 uptake.

3.2.2 Diurnal profiles

The CO_2 fluxes of rice, wheat, and maize during their growth periods show similar diurnal patterns, forming a typical U-shaped curve (Zhang et al., 2002). Nighttime NEE values remain positive and relatively stable due to continuous CO_2 release from crop and soil respiration, indicating that the ecosystem acts as a net CO_2 source. For all the three crops, NEE generally

https://doi.org/10.5194/egusphere-2026-2606
Preprint. Discussion started: 29 July 2026

shifts from positive to negative between 05:00 and 07:00, marking the transition from net emission to net uptake. During the daytime, CO_2 flux at the crop community scale is closely related to net radiation (Lafleur et al., 2001); increasing radiation enhances photosynthesis and respiration simultaneously (Yue et al., 2023), and when photosynthesis exceeds respiration, CO_2 uptake dominates (Guo et al., 2006).

For rice (Figure 9a), the daily NEE uptake peak reaches −1.116 gC m^{-2} h^{-1} at 11:00. Wheat (Figure 9b) shows a peak of −0.874 gC m^{-2} h^{-1} around 13:00. Maize (Figure 9c) reaches its peak uptake at 11:00, with a stronger intensity of −1.117 gC m^{-2} h^{-1}, likely due to the higher carbon assimilation efficiency and stomatal regulation capacity of C4 crops under high midday temperatures (Dwyer et al., 2007; Sage & Kubien, 2007). After noon, declining photosynthesis and reduced convective transport weaken CO_2 uptake (Wang et al., 2024), with NEE approaching zero near 18:00 around sunset (Li et al., 2006). The mismatch between the minimum NEE timing for rice and maize and the PAR peak may be related to excessive radiation increasing leaf temperature and partially inhibiting photosynthesis (Song et al., 2018). Overall, the three crops exhibit daytime CO_2 uptake and nighttime emission, although they differ in uptake intensity, transition timing, and duration of negative NEE values.

https://doi.org/10.5194/egusphere-2026-2606
Preprint. Discussion started: 29 July 2026

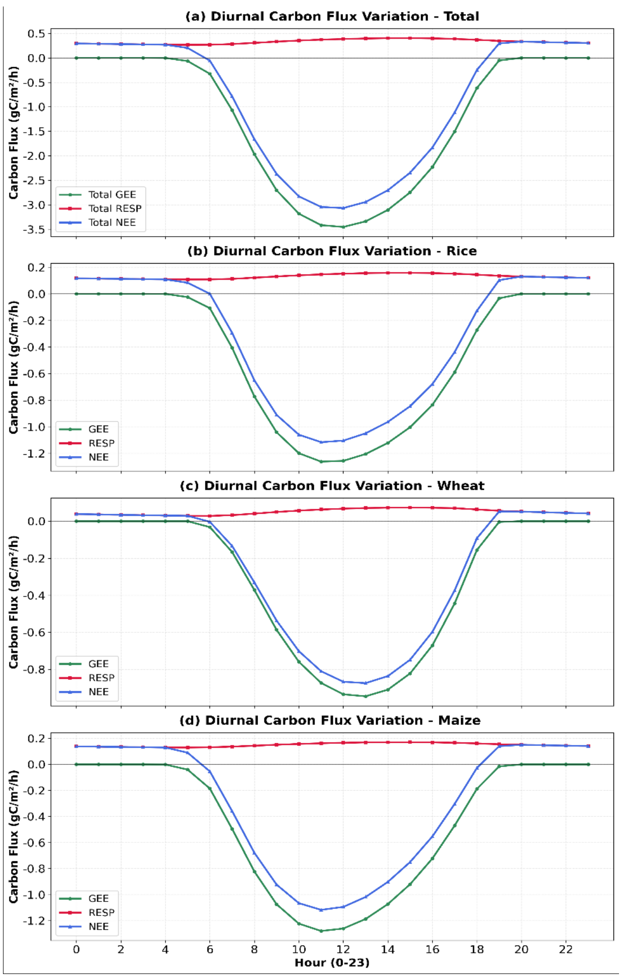

Figure 9. Diurnal carbon flux variations of three major crops. Simulated diurnal CO_2 fluxes (GEE, RESP, and NEE) for total crops **(a)**, rice **(b)**, wheat **(c)**, and maize **(d)**. Green, red, and blue lines represent gross primary production (GEE), ecosystem respiration (RESP), and net ecosystem exchange (NEE), respectively.

3.2.3 Daily profiles

Seasonal variations in photosynthesis, respiration, and atmospheric CO_2 fluxes of the three crops were simulated throughout the growing season together with changes in cultivated area (Figure 10). Based on day of year (DOY), the year was divided into four periods: DOY 60–

152, 153–244, 245–335, and 336–59, corresponding to spring, summer, fall, and winter, respectively. Rice generally grows from May to September, wheat mainly during spring, and maize from summer to September. Therefore, the following analysis focuses on the temporal variations of carbon fluxes and the corresponding planting areas during the crop growing periods.

Crop carbon fluxes show clear seasonal variability associated with crop phenology and planting area dynamics. At the early growth stage, planting areas are small and GEE, RESP, and NEE remain low, indicating weak CO_2 exchange with the atmosphere. Wheat (Figure 10c) enters rapid growth in early spring (DOY 61–120), initiating the earliest net CO_2 uptake of the year. Its maximum NEE reaches −3.36 TgC d^{-1} (DOY 115), with peak GEE and RESP of −3.69 TgC d^{-1} (DOY 118) and 0.54 TgC d^{-1} (DOY 122), respectively, while the planting area peaks at 233.44 × 10^3 km^2 (DOY 81). RESP is strongly influenced by crop growth and temperature but decreases in late spring due to low-temperature events (Zhang et al., 2020). During the late reproductive stage (DOY 121–155), GEE gradually declines while RESP remains relatively high, resulting in weaker CO_2 uptake (Yan et al., 2021; Wang et al., 2013). With increasing temperatures in summer, enhanced photosynthesis and canopy conductance strengthen atmospheric CO_2 uptake (Demyan et al., 2016). The planting areas of rice and maize expand rapidly, driving NEE to the strongest negative values of the year. For rice (Figure 10b), maximum NEE reaches −3.60 TgC d^{-1} (DOY 242), with peak GEE of −4.52 TgC d^{-1} and RESP of 1.06 TgC d^{-1} (DOY 226), while planting area peaks at 295.89 × 10^3 km^2 (DOY 193). Maize (Figure 10d), growing mainly from DOY 150–260, shows the strongest carbon uptake, with maximum NEE of −5.33 TgC d^{-1} (DOY 234), peak GEE of −6.81 TgC d^{-1}, RESP of 1.73 TgC d^{-1} (DOY 196), and planting area reaching 413.18 × 10^3 km^2 (DOY 185). Between DOY 203 and 248, the combined NEE of rice and maize falls below −6 TgC d^{-1}, representing the strongest nationwide crop carbon uptake (Figure 10a). As crops mature in fall, RESP declines rapidly

https://doi.org/10.5194/egusphere-2026-2606
Preprint. Discussion started: 29 July 2026

because soil respiration (RS) consists of heterotrophic respiration (RH) and autotrophic respiration (RA), with RA suppressed as root activity decreases (Zhang et al., 2013). The growing seasons end in late December (DOY 361) for rice, mid-June (DOY 170) for wheat, and late October (DOY 297) for maize, after which CO_2 fluxes return to baseline levels.

Daily mean CO_2 fluxes of rice, wheat, and maize show strong seasonal variability, with photosynthesis and respiration increasing to a peak and then gradually declining with crop development, environmental conditions, and management practices (Luo et al., 2020). Among the three crops, maize exhibits the largest seasonal fluctuations, consistent with observations from drip-irrigated maize fields in northwest China (Guo et al., 2021). Peak GEE and NEE for maize exceed those of wheat (Falge et al., 2002; Tao et al., 2022), mainly because C4 plants have higher light-use efficiency than C3 plants (Hollinger et al., 2005) and grow under warmer and wetter conditions (Wang et al., 2015). Consequently, maize shows stronger carbon uptake than wheat and rice. The temporal evolution of planting areas closely corresponds to CO_2 flux dynamics, highlighting the important role of agricultural activities in regulating the regional carbon cycle.

The simulated daily NEE peaks were further compared with previous observational studies. Eddy covariance measurements reported maximum daily carbon uptake of −10.63 g C m^{-2} d^{-1} for rice in the Yangtze River Delta (Sun et al., 2015) and −10 ± 1 g C m^{-2} d^{-1} in the Huai River Basin (Zhang et al., 2025). In South Korea, peak rice NEE reached −15.4 ± 2.2 μmol m^{-2} s^{-1} (approximately −13.7 to −15.8 g C m^{-2} d^{-1}; Lindner et al., 2015), while UAV-based biochemical modeling estimated −12.08 g C m^{-2} d^{-1} for rice fields in Shanghai (Hu et al., 2024). The value derived in this study corresponds to −12.17 g C m^{-2} d^{-1}. For wheat, cumulative NEE of −627 g C m^{-2} was reported in Germany (Schmidt et al., 2012), which is close to the annual value of −626 g C m^{-2} yr^{-1} estimated in this study. Peak daily uptake values have been reported as −12.88 g C m^{-2} d^{-1} in the Yangtze River Delta (Sun et al., 2015), −14.6 g C m^{-2} d^{-1} in the

https://doi.org/10.5194/egusphere-2026-2606
Preprint. Discussion started: 29 July 2026

Guanzhong Plain (Peng et al., 2023), and −10 to −13 g C m^{-2} d^{-1} in the North China Plain (Lei and Yang, 2010), whereas this study estimates −14.4 g C m^{-2} d^{-1}. For maize, minimum daily NEE in the North China Plain ranges from −11 to −15 g C m^{-2} d^{-1} (Lei and Yang, 2010) and −10 to −13 g C m^{-2} d^{-1} in other studies (Li et al., 2006), while observations in the United States report −12 to −19 g C m^{-2} d^{-1} (Hollinger et al., 2005). The value derived in this study is −12.9 g C m^{-2} d^{-1}. Overall, these estimates agree well with previous studies, and remaining differences may result from variations in crop management practices, climatic conditions, soil properties, growing season length, and crop types (Chen et al., 2015).

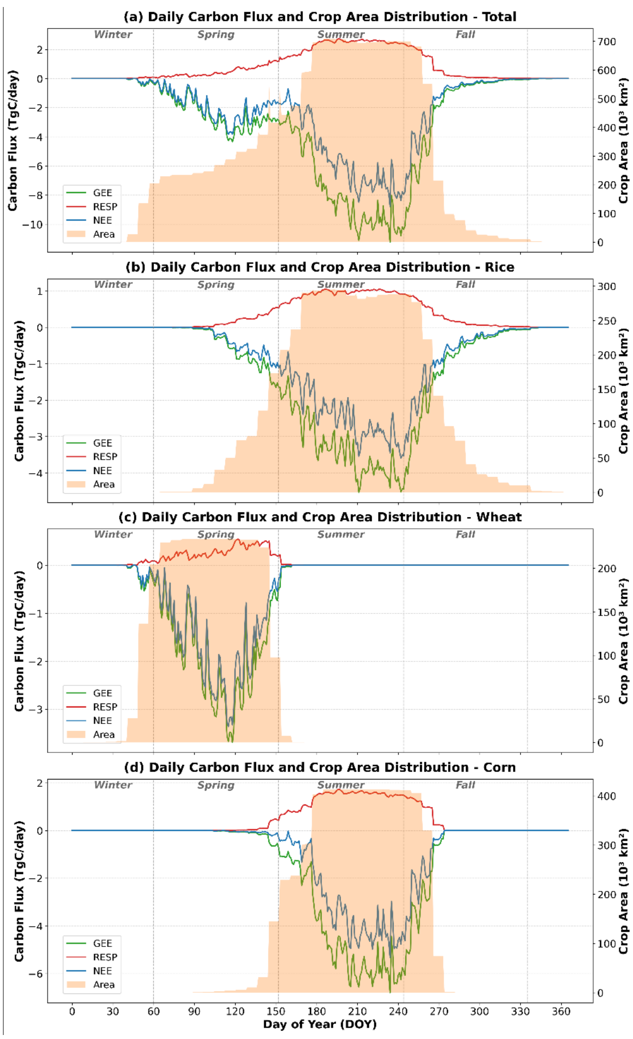

https://doi.org/10.5194/egusphere-2026-2606
Preprint. Discussion started: 29 July 2026

Figure 10. Daily carbon fluxes and crop area for major crops in China. Simulated daily CO_2 fluxes (GEE, RESP, and NEE) and cultivated area for total crops **(a)**, rice **(b)**, wheat **(c)**, and maize **(d)**. Green, red, and blue lines denote GEE, RESP, and NEE, respectively. Orange shading indicates cultivated area.

3.3 Relationships between NEE and grain yields

Since grain yield is derived from crop carbon uptake, crop yield serves as a practical indicator for evaluating NEE (Qader et al., 2018; Wang et al., 2019). To examine the relationship between carbon uptake and crop yield at the regional scale, provincial NEE of rice, wheat, and maize was calculated for five even years (2014, 2016, 2018, 2020, and 2022) based on simulated annual mean NEE across 29 provinces in China (excluding Xinjiang and Xizang). Correlation analysis was conducted between provinces with |NEE| > 0 and corresponding crop yield data from the National Bureau of Statistics (https://www.stats.gov.cn/sj/ndsj/). The numbers of valid samples were 119 for rice, 50 for wheat, and 105 for maize, all showing significant positive correlations ($p < 0.001$). Wheat exhibited the strongest relationship (r = 0.982), indicating strong synchronization between carbon uptake and yield formation in major producing regions (Figure 11b). Rice showed a slightly weaker but still strong correlation (r = 0.818) with more dispersed data points (Figure 11a), while maize also displayed a strong relationship (r = 0.869) (Figure 11c).

https://doi.org/10.5194/egusphere-2026-2606
Preprint. Discussion started: 29 July 2026

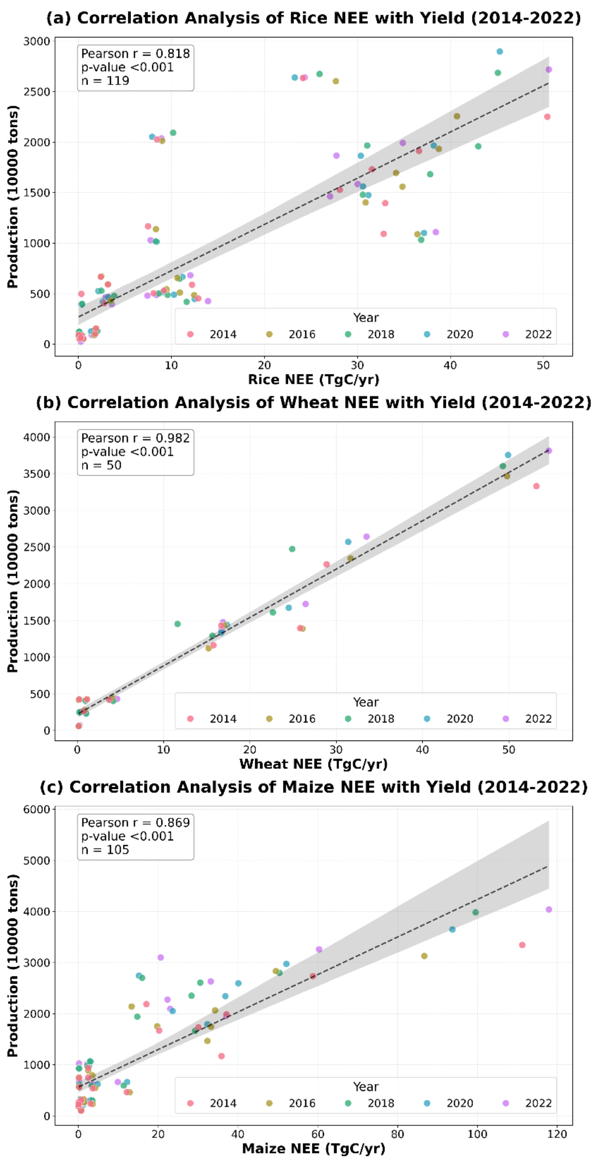

Figure 11. Correlations between simulated NEE and crop yield across Chinese provinces. Provincial relationships between annual NEE and statistical yield for rice **(a)**, wheat **(b)**, and maize **(c)** during 2014–2022. Only provinces with nonzero NEE are included. Gray shading indicates the 95% confidence interval, and the black dashed line represents the fitted regression.

https://doi.org/10.5194/egusphere-2026-2606
Preprint. Discussion started: 29 July 2026

To further examine the relationship between regional carbon uptake and crop yield, the simulated annual NEE of rice, wheat, and maize in 2020 was ranked for the top ten producing provinces and compared with provincial yield statistics (Figure 12). The highest rice NEE occurred in Heilongjiang (45.31 TgC yr^{-1}), corresponding to the largest yield (2896.2 × 10^4 t). Heilongjiang and Hunan together contributed about 22.2% of China's rice NEE, close to the 24.6% estimated using the DNDC model (Lu et al., 2024). Jiangsu and Guangdong followed with NEE values of 38.21 and 37.17 TgC yr^{-1}, consistent with the strong CO_2 uptake capacity of cropland vegetation in Jiangsu (Weng et al., 2018). However, in traditional rice-producing regions such as Hunan and Sichuan, the NEE ranking does not fully correspond to yield, particularly between Guangdong and Hunan, indicating regional differences and potential over- or underestimation (Figure 12a).

For wheat, the highest NEE values occur in Henan (49.92 TgC yr^{-1}) and Shandong (31.39 TgC yr^{-1}), with yields of 3753.1 × 10^4 t and 2568.9 × 10^4 t, respectively, showing a relatively linear relationship (Figure 12b). For maize, NEE in Hebei (23.63 TgC yr^{-1}) and Inner Mongolia (15.20 TgC yr^{-1}) corresponds to yields of 2051.8 × 10^4 t and 2742.7 × 10^4 t, showing larger deviations, whereas other provinces are more consistent (Figure 12c). Overall, the NEE–yield relationship is strongest for wheat, while larger provincial differences exist for rice and maize. The total NEE of the three crops is highest in Heilongjiang (39.09 TgC yr^{-1}), followed by Henan, Shandong, and Anhui, consistent with the spatial distribution of China's major grain-producing regions (Figure 12d). Regions with high NEE are mainly located in provinces with favorable light, heat, and water conditions that enhance photosynthetic carbon uptake (Wang et al., 2021; Zhang et al., 2025). Crop NEE is also influenced by planting scale and farmland management. Provinces with abundant cropland and higher precipitation generally have lower irrigation costs (Wang et al., 2015; Xin et al., 2011), while higher mechanization improves labor productivity (Cai et al., 2016). In addition, policies such as agricultural tax exemptions,

https://doi.org/10.5194/egusphere-2026-2606
Preprint. Discussion started: 29 July 2026

subsidies, and minimum purchase prices promote grain production (Long et al., 2014), indirectly supporting planting expansion and carbon uptake.

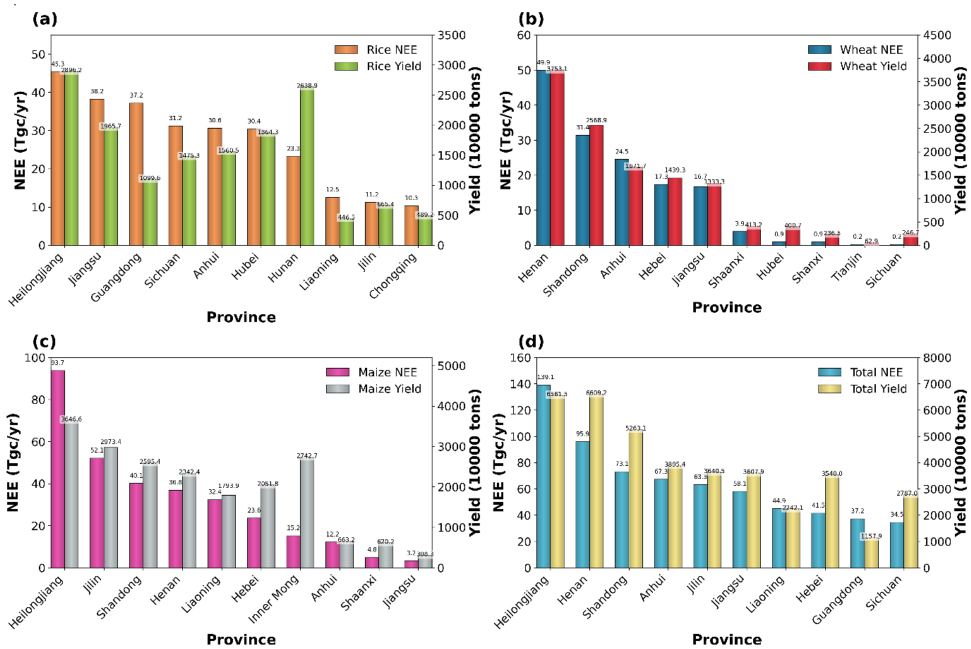

Figure 12. Comparison of simulated annual NEE and statistical crop yield for major crops across China in 2020. Provincial comparisons for rice **(a)**, wheat **(b)**, maize **(c)**, and their total **(d)**. Bars represent NEE (TgC yr^{-1}) and yield (10^4 t) for the top ten producing provinces.

3.4 Model uncertainty analysis

3.4.1 Limitations of the four VPRM parameters

Differences in the NEE–yield relationship among crops largely reflect the limited regional universality of the four key VPRM parameters (λ, PAR_0, α, β) at the national scale. Strong climatic contrasts between northern and southern China create large differences in radiation, temperature, and moisture conditions, which directly affect crop photosynthesis and respiration. However, national simulations usually apply fixed parameter settings that cannot fully capture regional variability in crop physiological traits. In the VPRM-CHINA model (Dayalu et al.,

https://doi.org/10.5194/egusphere-2026-2606
Preprint. Discussion started: 29 July 2026

2018), parameters for maize and wheat have been partly calibrated using observations in China, whereas rice parameters still largely rely on empirical grassland-based values. Although rice parameters were adjusted in this study, they were derived from the Changling flux tower in Northeast China, a single-cropping and cool-climate region, and therefore cannot represent double-cropping rice systems in southern China. Consequently, simulated rice NEE agrees relatively well with yield in Northeast China (e.g., Heilongjiang and Jilin) but tends to be underestimated in East and South China (e.g., Jiangsu and Guangdong) (Figure 12a). Rice and maize also span multiple climatic zones with substantial differences in photosynthetic and respiration characteristics, so uniform parameters may perform well in some regions but deviate in others (Figure 12a, c). By contrast, wheat is mainly concentrated in the North China Plain, where climatic conditions are relatively homogeneous, allowing parameters derived from regional flux towers to better represent crop ecosystems and produce stronger agreement between simulated NEE and yield (Figure 12b). These results indicate that parameters derived from limited sites are insufficient for representing national-scale crop ecosystems.

The VPRM parameters are also a major source of uncertainty in NEE simulations because they represent vegetation photosynthetic efficiency, radiation response, and respiration characteristics, which vary across regions and seasons. Flux observations are therefore essential for parameter optimization. For example, Zhang et al. (2017) optimized parameters for temperate broadleaf and Korean pine forests using data from the CBS Changbai Mountain flux tower, while Liu et al. (2014) calibrated parameters for subtropical evergreen needleleaf forests using data from the Qianyanzhou site, improving regional NEE simulations. Nevertheless, even within North America, parameters derived from different flux towers for the same land-use type show clear discrepancies (Hilton et al., 2013), and parameters selected using MODIS land-cover data may also vary across regions (Diao et al., 2015). In addition, VPRM simplifies ecosystem respiration as a linear function of temperature, whereas respiration

https://doi.org/10.5194/egusphere-2026-2606
Preprint. Discussion started: 29 July 2026

is influenced by multiple biological and abiotic processes, which further increases NEE uncertainty. More realistic formulations, such as parameterizing respiration using both EVI and temperature, may therefore improve model performance.

Parameter optimization is further constrained by the limited availability of flux tower observations. The Korean Peninsula lacks sufficient flux measurements across vegetation types and therefore relies on the default VPRM parameters (Park et al., 2020). Flux towers are also sparse in Northeast China (Li et al., 2020), where parameters are often adopted from calibrations based on 65 eddy-covariance towers in North America (Hilton et al., 2013). In contrast, European ecosystem parameters are derived from 46 flux towers distributed across the continent (Gerbig & Koch, 2023). Because long-term flux observations in China remain limited and unevenly distributed, region-specific parameters for different crop systems cannot yet be independently derived. Applying uniform parameters nationwide therefore overlooks regional differences in climate and vegetation phenology, reducing model accuracy across regions. Expanding long-term flux observation networks in diverse climatic zones and major crop-producing regions will enable the development of regionally differentiated VPRM parameter schemes, improving the representation of spatial heterogeneity in climate and vegetation phenology and enhancing national-scale simulations.

3.4.2 Spatial mismatch between fragmented cropland and model resolution

The deviation between NEE and yield is also related to model spatial resolution and farmland distribution. The WRF-VPRM simulations use a spatial resolution of 9 km×9 km, whereas statistical yield is calculated based on actual arable land area, leading to scale mismatches. In southern China, farmland is highly fragmented and interspersed with forests, water bodies, and other land uses. Under coarse-resolution grids, the averaging effect can dilute crop pixels and underestimate regional NEE. For example, in Hunan, where rice yields are high,

https://doi.org/10.5194/egusphere-2026-2606
Preprint. Discussion started: 29 July 2026

simulated NEE is relatively low, suggesting that grid averaging obscures the CO_2 uptake of high-yield rice fields. In contrast, farmland in Northeast and North China is more continuous, allowing cropland to occupy a larger proportion of grid cells and enabling model outputs to better reflect yield patterns.Higher model resolution can better capture fine-scale features (Geels et al., 2007). Simulations with spatial resolutions of 36 km, 12 km, and 4 km show that the 4 km grid more accurately reproduces the spatiotemporal evolution of CO_2 concentrations (Mai et al., 2024), but this entails significantly higher computational costs. Similarly, Ballav et al. (2012) reported that low horizontal and vertical resolutions in the WRF-CO_2 model cannot adequately represent the complex coastline and topography of the Japanese archipelago. Future improvements in simulating crop CO_2 flux–yield relationships could therefore involve increasing driving data resolution to 1 km and developing sub-grid parameterization schemes for fragmented farmland in VPRM to better represent photosynthesis and respiration in heterogeneous croplands.

3.4.3 Uncertainty in meteorological forcing

Meteorological uncertainty is another important source of bias in the simulations of NEE because meteorological fields directly control photosynthesis and respiration processes. In the model, GEE and RESP depend on key variables such as temperature and radiation; therefore, biases in these fields influence daily and seasonal NEE by altering photosynthetic efficiency, stomatal activity, and respiration rates. Since VPRM flux calculations rely on the atmospheric state simulated by the regional WRF model, uncertainties in initial and boundary conditions can propagate during model integration and affect flux simulations (Ki and Kim et al., 2021). Transport processes in WRF, particularly advection and vertical mixing, also strongly influence CO_2 distributions. Vertical mixing affects the vertical structure of CO_2 concentrations, while

https://doi.org/10.5194/egusphere-2026-2606
Preprint. Discussion started: 29 July 2026

wind-driven transport controls their spatial and temporal variability within the planetary boundary layer (Pillai et al., 2011). These processes may further modify the meteorological background affecting surface ecological processes and thus indirectly influence NEE estimates.

Radiation is a key driver of photosynthesis, but cumulus clouds under convective conditions are not always accurately represented in WRF. Biases in the radiation field can therefore lead to significant simulation errors (Ahmadov et al., 2007). For example, Diao et al., (2015) reported that WRF overestimated cloud cover in the study region, resulting in underestimated surface shortwave radiation and consequently lower simulated air temperature, which may further bias NEE estimates (Mahadevan et al., 2008; Jamroensan et al., 2013). In addition, (Li et al., 2020) showed through offline VPRM simulations that biases in PAR exert a stronger influence on daily GEE than biases in air temperature.

To reduce meteorology-driven uncertainties in NEE simulations, improvements are needed in vertical mixing, turbulence, boundary-layer, and cumulus–radiation parameterization schemes. Assimilation of ground observations and satellite data could also help constrain key meteorological variables such as temperature and radiation during simulations. Combined with multi-site and multi-year NEE validation, these improvements would enhance the accuracy and reliability of the WRF-VPRM simulations.

4 Conclusions

This study applied the WRF-VPRM model to quantify GEE, RESP, and NEE for three major crops (rice, wheat, and maize) in central and eastern China, highlighting the important role of agricultural ecosystems in the regional carbon cycle. Cropland exhibits strong net CO_2 uptake during the growing season, with national GEE, RESP, and NEE of approximately 1084.7, 305.5, and 779.2 TgC yr^{-1}, respectively. Rice, wheat, and maize contribute 39.6%, 18.8%, and 41.7% of total CO_2 fixation, indicating that maize and rice dominate carbon uptake in China's cropland ecosystems. Spatially, CO_2 fixation by maize and wheat is concentrated in the Northeast and North China Plains, whereas rice fixation mainly occurs in the middle and lower reaches of the Yangtze River, making these regions the core areas of agricultural CO_2 uptake in China.

CO_2 fluxes show clear diurnal and seasonal patterns, characterized by daytime uptake and nighttime release. Peak NEE values for rice, wheat, and maize are −1.12, −0.87, and −1.12 gC m^{-2} h^{-1}, occurring at approximately 11:00, 13:00, and 11:00, respectively. During the growing season, GEE and RESP increase with crop development and reach maxima in summer. Maximum daily GEE values are −4.52, −3.69, and −6.81 TgC d^{-1} for rice (DOY 242), wheat (DOY 118), and maize (DOY 234), while peak RESP values are 1.06 (DOY 226), 0.54 (DOY 122), and 1.73 TgC d^{-1} (DOY 196), respectively. Wheat reaches its earliest NEE peak (−3.36 TgC d^{-1}) in spring at DOY 115, whereas rice and maize peaks (−3.60 and −5.33 TgC d^{-1}) occur in summer at DOY 242 and 234. The growth periods end in late December (DOY 361) for rice, mid–late June (DOY 170) for wheat, and late October (DOY 297) for maize.

The WRF-VPRM model reasonably reproduces the spatiotemporal variability of crop CO_2 fluxes in central and eastern China. Provincial NEE is significantly correlated with statistical yield ($p < 0.001$), with correlation coefficients of 0.982 for wheat, 0.818 for rice, and 0.869 for maize, although discrepancies exist in some provinces. Model uncertainties mainly arise from VPRM parameters, spatial resolution, and meteorological inputs. Future work should reduce meteorological simulation errors, apply region-specific VPRM parameters, and develop improved agricultural sub-grid parameterization schemes to enhance the accuracy and spatial adaptability of crop CO_2 flux simulations.

Code and data availability

The observational data used in this study and revised VPRM module in the model are available at https://doi.org/10.5281/zenodo.15859715 (Feng, 2026). The anthropogenic CO_2

emission inventory is from the MEIC inventory that is available at http://www.meicmodel.org. Satellite data of MODIS EVI and LSWI are calculated online at the Google Earth Engine (GEE) platform (https://code.earthengine.google.com/). The meteorological data driving the model are from the NCEP FNL analysis (http://rda.ucar.edu/datasets/ds083.2/). CO_2 initial and boundary conditions for the model are interpolated from the Jena CarboScope estimate (https://www.bgc-jena.mpg.de/CarboScope/). The source code of the model is accessible at http://vqp2qrae.xiaomy.net:29988/#code.

Author contribution

TF conceptualized the ideas, verified the conclusions, and revised the paper. JY performed the simulation, processed the data, and prepared the data visualization. JY and TF designed the experiments and prepared the paper with contributions from all authors. CW and HX provided observational data. SZ, WL, and LW analyzed the study data and reviewed the paper. GY and WS provided critical reviews on this study.

Competing interests

The authors have no competing interests.

Acknowledgments

This research has been supported by the National Natural Science Foundation of China (Grants 42371080 and 42371093), the Ningbo Young Leading Talent Program for Science and Technology Innovation (Grant 2025QL045), and the High-level Scientific and Technological Project of Ningbo University (Grant No. GJPY2026022).

References

Entekhabi, D.: Recent advances in land-atmosphere interaction research, Rev. Geophys., 33, 995–1003, https://doi.org/10.1029/95RG01163, 1995.

Schmidt, M., Reichenau, T. G., Fiener, P., and Schneider, K.: The carbon budget of a winter wheat field: an eddy covariance analysis of seasonal and inter-annual variability, Agric. For. Meteorol., 165, 114–126, https://doi.org/10.1016/j.agrformet.2012.05.012, 2012.

Søgaard, H., Jensen, N. O., Bøgh, E., Hasager, C. B., Schelde, K., and Thomsen, A.: Carbon dioxide exchange over agricultural landscape using eddy correlation and footprint modelling, Agric. For. Meteorol., 114, 153–173, https://doi.org/10.1016/S0168-1923(02)00177-6, 2003.

https://doi.org/10.5194/egusphere-2026-2606
Preprint. Discussion started: 29 July 2026

Mauder, M., Cuntz, M., Drüe, C., Ackermann, M., Delpierre, N., Erbs, A., Foken, T., Hammerle, A., Heinesch, B., Hörtnagl, L., Ibrom, A., Knohl, A., Laurens, A., Levula, J., Munger, J. W., Rebmann, C., Schmid, G. P., Sermondadaz, G., and Wohlfahrt, G.: A strategy for quality and uncertainty assessment of long-term eddy-covariance measurements, Agric. For. Meteorol., 169, 122–135, https://doi.org/10.1016/j.agrformet.2012.09.006, 2013.

Béziat, P., Ceschia, E., and Dedieu, G.: Carbon balance of a three crop succession over two cropland sites in South West France, Agric. For. Meteorol., 149, 1628–1645, https://doi.org/10.1016/j.agrformet.2009.05.004, 2009.

Yu, G., Wen, X., Sun, X., Tanner, B. D., Lee, X., and Chen, J.: Overview of ChinaFLUX and evaluation of its eddy covariance measurement, Agr. Forest Meteorol., 137, 125–137, https://doi.org/10.1016/j.agrformet.2006.02.011, 2006.

Peters, W., Jacobson, A. R., Sweeney, C., Andrews, A. E., Conway, T. J., Masarie, K., Miller, J. B., Bruhwiler, L. M. P., Pétron, G., Hirsch, A. I., Worthy, D. E. J., van der Werf, G. R., Randerson, J. T., Wennberg, P. O., Krol, M. C., and Tans, P. P.: An atmospheric perspective on North American carbon dioxide exchange: CarbonTracker, Proc. Natl. Acad. Sci. USA, 104, 18925–18930, https://doi.org/10.1073/pnas.0708986104, 2007.

Shi, Z., Crowell, S., Luo, Y., and Moore III, B.: Model structures amplify uncertainty in predicted soil carbon responses to climate change, Nat. Commun., 9, 2171, https://doi.org/10.1038/s41467-018-04526-9, 2018.

Ahmadov, R., Gerbig, C., Kretschmer, R., Körner, S., Neininger, B., Modi, A. J., Canonici, J.-C., and Heimann, M.: Mesoscale covariance of transport and CO_2 fluxes: evidence from observations and simulations using the WRF-VPRM coupled atmosphere-biosphere model, J. Geophys. Res.-Atmos., 112, D22106, https://doi.org/10.1029/2007JD008552, 2007.

Jamroensan, A.: Improving bottom-up and top-down estimates of carbon fluxes in the Midwestern USA, PhD thesis, University of Iowa, Iowa City, USA, http://ir.uiowa.edu/etd/2530, 2013.

Huggannavar, V. and Indu, J.: Coupled weather-biosphere model (WRF-VPRM) response to extreme land cover scenarios over Ganga basin: a cross-component analysis, Environ. Res. Commun., 5, 085006, https://doi.org/10.1088/2515-7620/acea1e, 2023.

San José, R., Perez-Camanyo, J. L., and Jimenez-Gañan, M.: Assessing future greenhouse gas concentrations in Madrid, Spain: a dynamical downscaling approach using WRF-VPRM, Air Qual. Atmos. Hlth., https://doi.org/10.1007/s11869-025-01798-1, 2025.

Hilton, T. W., Davis, K. J., Keller, K., and Urban, N. M.: Improving North American terrestrial CO_2 flux diagnosis using spatial structure in land surface model residuals, Biogeosciences, 10, 4607–4625, https://doi.org/10.5194/bg-10-4607-2013, 2013.

Park, C., Gerbig, C., Newman, S., Ahmadov, R., Feng, S., Gurney, K. R., Carmichael, G. R., Park, S.-Y., Lee, H.-W., Goulden, M., Stutz, J., Peischl, J., and Ryerson, T.: CO_2 transport, variability, and budget over the Southern California Air Basin using the high-resolution WRF-VPRM model during the CalNex 2010 campaign, J. Appl. Meteorol. Climatol., 57, 1337–1352, https://doi.org/10.1175/JAMC-D-17-0358.1, 2018.

Wang, Y., Liu, S., and Shi, H.: Comparison of climate change impacts on the growth of C3 and C4 crops in China, Ecol. Inform., 74, 101968, https://doi.org/10.1016/j.ecoinf.2022.101968, 2023.

Kumar, A., Nayak, A. K., Hanjagi, P. S., Kumari, K., Vijayakumar, S., Mohanty, S., Tripathi, R., and Panneerselvam, P.: Submergence stress in rice: Adaptive mechanisms, coping strategies and future research needs, Environ. Exp. Bot., 186, 104448, https://doi.org/10.1016/j.envexpbot.2021.104448, 2021.

Mahadevan, P., Wofsy, S. C., Matross, D. M., Braswell, B. H., Hamze, A. L., Eluszkiewicz, J., McKain, M. E., and Lin, J. C.: A satellite-based biosphere parameterization for net ecosystem CO_2 exchange: Vegetation Photosynthesis and Respiration Model (VPRM), Global Biogeochem. Cy., 22, GB2005, https://doi.org/10.1029/2006GB002735, 2008.

Huete, A., Didan, K., Miura, T., Rodriguez, E. P., Gao, X. Y., and Ferreira, L. G.: Overview of the radiometric and biophysical performance of the MODIS vegetation indices, Remote Sens. Environ., 83, 195–213, https://doi.org/10.1016/S0034-4257(02)00096-2, 2002.

Jiang, Z. Y., Huete, A. R., Didan, K., and Miura, T.: Development of a two-band enhanced vegetation index without a blue band, Remote Sens. Environ., 112, 3833–3845, https://doi.org/10.1016/j.rse.2008.06.006, 2008.

Dayalu, A., Munger, J. W., Wofsy, S. C., Wang, Y., Nehrkorn, T., Zhao, Y., McElroy, M. B., Nielsen, C. P., and Lu, H.: Assessing biotic contributions to CO_2 fluxes in northern China using the Vegetation, Photosynthesis and Respiration Model (VPRM-CHINA) and observations from 2005 to 2009, Biogeosciences, 15, 6713–6729, https://doi.org/10.5194/bg-15-6713-2018, 2018.

Xiao, X., Hollinger, D., Aber, J., Goltz, M., Davidson, E. A., Zhang, Q., and Moore, B.: Modeling gross primary production of temperate deciduous broadleaf forest using satellite images and climate data, Remote Sens. Environ., 91, 256–270, https://doi.org/10.1016/j.rse.2004.03.010, 2004.

Chandrasekar, K., Sesha Sai, M. V. R., Roy, P. S., and Dwevedi, R. S.: Land Surface Water Index (LSWI) response to rainfall and NDVI using the MODIS Vegetation Index product, Int. J. Remote Sens., 31, 3987–4005, https://doi.org/10.1080/01431160802575653, 2010.

Vermote, E. F., Justice, C. O., Claverie, M., and Franch, B.: MODIS Surface Reflectance Climate Data Record Products: Algorithm Theoretical Basis Document (ATBD) Version 6. NASA Goddard Space Flight Center, Greenbelt, MD, 2021.

Hill, M. J., Dymond, J. R., and Shepherd, J. D.: Using MODIS MOD09A1 Surface Reflectance Data to Monitor Vegetation Recovery Following Wildfire, Int. J. Remote Sens., 41, 8543–8562, https://doi.org/10.1080/01431161.2020.1776234, 2020.

Jung, M., Henkel, K., Herold, M., and Churkina, G.: Exploiting synergies of global land cover products for carbon cycle modeling, Remote Sens. Environ., 101, 534–553, https://doi.org/10.1016/j.rse.2006.01.020, 2006.

Feng, T.: Code and data for “Development and evaluation of a crop-specific WRF-VPRM framework: Integrating dynamic phenology and high-resolution distributions for agricultural CO_2 exchange in China”, Zenodo, https://doi.org/10.5281/zenodo.15859715, 2026.

Luo, Y., Zhang, Z., Chen, Y., Li, Z., and Tao, F.: ChinaCropPhen1km: a high-resolution crop

https://doi.org/10.5194/egusphere-2026-2606
Preprint. Discussion started: 29 July 2026

phenological dataset for three staple crops in China during 2000–2015 based on leaf area index (LAI) products, Earth Syst. Sci. Data, 12, 197–214, https://doi.org/10.5194/essd-12-197-2020, 2020.

Rödenbeck, C., Houweling, S., Gloor, M., and Heimann, M.: CO_2 flux history 1982–2001 inferred from atmospheric data using a global inversion of atmospheric transport, Atmos. Chem. Phys., 3, 1919–1964, https://doi.org/10.5194/acp-3-1919-2003, 2003.

Li, M., Zhang, Q., Streets, D. G., He, K. B., Cheng, Y. F., Emmons, L. K., Huo, H., Kang, S. C., Lu, Z., Shao, M., Su, H., Yu, X., and Zhang, Y.: Anthropogenic emission inventories in China: A review, Natl. Sci. Rev., 4, 834–866, https://doi.org/10.1093/nsr/nwx150, 2017.

Cintineo, J. M., Van Weverberg, K., Morrison, H., and Milbrandt, J. A.: Evaluation of the WRF Single-Moment 6-Class Microphysics Scheme (WSM6) Using Observations from Two Cold-Season IOPs, Mon. Weather Rev., 142, 4223–4244, 2014.

Janjić, Z. I.:Nonsingular implementation of the Mellor–Yamada level 2.5 scheme in the NCEP Meso model. NCEP office note 1–61, 2002.

Yee, J. H., Chen, S. H., and Hong, S. Y.: A Modified Surface Layer Parameterization for Mesoscale Models Based on Monin-Obukhov Similarity Theory, Mon. Weather Rev., 126, 3083–3101, 1998.

Chen, F. and Dudhia, J.: Coupling an advanced land surface-hydrology model with the Penn State-NCAR MM5 modeling system. Part II: Preliminary model validation, Mon. Weather Rev., 129, 587–604, https://doi.org/10.1175/1520-0493(2001)129<0569:CAALSH>2.0.CO;2, 2001.

Dudhia, J.: Numerical study of convection observed during the winter monsoon experiment using a mesoscale two-dimensional model, J. Atmos. Sci., 46, 3077–3107, https://doi.org/10.1175/1520-0469(1989)046<3077:NSOCOD>2.0.CO;2, 1989.

Mlawer, E. J., Taubman, S. J., Brown, P. D., Iacono, M. J., and Clough, S. A.: Radiative transfer for inhomogeneous atmospheres: RRTM, a validated correlated-k model for the longwave, J. Geophys. Res.-Atmos., 102, 16663–16682, https://doi.org/10.1029/97JD00237, 1997.

Kain, J. S.: The Kain–Fritsch convective parameterization: An update, J. Appl. Meteorol., 43, 170–181, https://doi.org/10.1175/1520-0450(2004)043<0170:TKCPAU>2.0.CO;2, 2004.

Wesely, M. L.: Parameterization of surface resistances to gaseous dry deposition in regional-scale numerical models, Atmos. Environ., 23, 1293–1304, https://doi.org/10.1016/0004-6981(89)90153-4, 1989.

Dong, G., Wang, Y., Wang, K., Jiang, S. and Shao, C.: A dataset of carbon and water fluxes in the Changling alkali-saline paddy rice fields in the Songnen Plain, China (2018 –2020), Science Data Bank https://doi.org/10.57760/sciencedb.o00119.00068, 2022.

Zhou, L., Geng, J., Zhou, G., Zhang, S., and Wu, Y.: A dataset of carbon and water fluxes in the wheat and summer maize rotation ecosystem at Gucheng Station (2020–2022), Science Data Bank, https://doi.org/10.11922/11-6035.csd.2023.0022.zh, 2023.

Zhang, F., Li, H., Zhang, L., Li, J., Yang, Y., Yu, G., and Li, Y.: A dataset of the observations of carbon, water and heat fluxes over an alpine shrubland in Haibei (2011–2020), China Sci. Data, 8, https://doi.org/10.11922/11-6035.csd.2023.0013.zh, 2023.

Xu, Z., Liu, S., Che, T., Ren, Z., Tan, J., and Zhang, Y.: A dataset of carbon-water vapor fluxes

and meteorological observations in the middle and lower reaches of Heihe river basin from 2013 to 2022, China Sci. Data, 9, 1–12, https://doi.org/10.11922/11-6035.csd.2024.0099.zh, 2024.
Xu, Z., Liu, S., Li, X., Xu, T., and Zhu, Z.: Water vapor-heat-carbon fluxes and meteorological observation matrix dataset in 2012 over Zhangye oasis-desert area, China Sci. Data, 8, https://doi.org/10.11922/11-6035.csd.2023.0035.zh, 2023.
Du, J., Luo, W., An, Z., Zhang, L., Huang, H., Hao, Y., and Wang, Y.: A dataset of carbon and water flux observations from typical ecosystems in the mountainous and hilly region of the Yan Mountains, Beijing, from 2020 to 2021, China Sci. Data, 8, 1–9, https://doi.org/10.11922/11-6035.csd.2023.0030.zh, 2023.
Connor, B. J., Boesch, H., Toon, G., Sen, B., Miller, C., and Crisp, D.: Orbiting Carbon Observatory: Inverse method and prospective error analysis, J. Geophys. Res.-Atmos., 113, D05305, https://doi.org/10.1029/2006JD008336, 2008.
Laughner, J. L., Toon, G. C., Mendonca, J., Petri, C., Roche, S., Wunch, D., Blavier, J.-F., Griffith, D. W. T., Heikkinen, P., Keeling, R. F., Kiel, M., Kivi, R., Roehl, C. M., Stephens, B. B., Baier, B. C., Chen, H., Choi, Y., Deutscher, N. M., DiGangi, J. P., Gross, J., Herkommer, B., Jeseck, P., Laemmel, T., Lan, X., McGee, E., McKain, K., Miller, J., Morino, I., Notholt, J., Ohyama, H., Pollard, D. F., Rettinger, M., Riris, H., Rousogenous, C., Sha, M. K., Shiomi, K., Strong, K., Sussmann, R., Té, Y., Velazco, V. A., Wofsy, S. C., Zhou, M., and Wennberg, P. O.: The Total Carbon Column Observing Network's GGG2020 data version, Earth Syst. Sci. Data, 16, 2197–2260, https://doi.org/10.5194/essd-16-2197-2024, 2024.
Jacobson, A. R., Basu, S., Thoning, K. W., Peters, W., and Tans, P. P.: CarbonTracker CT2022, NOAA Global Monitoring Laboratory, https://gml.noaa.gov/ccgg/carbontracker/, 2023.
Baldocchi, D.: Breathing of the terrestrial biosphere: lessons learned from a global net work of carbon dioxide flux measurement systems, Aust. J. Bot., 56, 1–26, https://doi.org/10.1071/BT07151, 2008.
Chevallier, F., Remaud, M., O'Dell, C. W., Baker, D., Peylin, P., and Cozic, A.: Objective evaluation of surface- and satellite-driven carbon dioxide atmospheric inversions, Atmos. Chem. Phys., 19, 14233–14251, https://doi.org/10.5194/acp-19-14233-2019, 2019.
Liu, J., Baskaran, L., Bowman, K., Schimel, D., Bloom, A. A., Parazoo, N. C., Oda, T., Carroll, D., Menemenlis, D., Joiner, J., Commane, R., Daube, B., Gatti, L. V., McKain, K., Miller, J., Stephens, B. B., Sweeney, C., and Wofsy, S.: Carbon Monitoring System Flux Net Biosphere Exchange 2020 (CMS-Flux NBE 2020), Earth Syst. Sci. Data, 13, 299–330, https://doi.org/10.5194/essd-13-299-2021, 2021.
Zhou, L., Conway, T. J., White, J. W. C., Mukai, H., Zhang, X., Wen, Y., Li, J., and MacClune, K.: Long-term record of atmospheric CO_2 and stable isotopic ratios at Waliguan Observatory: Background features and possible drivers, 1991–2002, Global Biogeochem. Cy., 19, GB3021, https://doi.org/10.1029/2004GB002430, 2005.
Ciais, P., Sabine, C., Bala, G., Bopp, L., Brovkin, V., Canadell, J., Chhabra, A., DeFries, R., Galloway, J., Heimann, M., Jones, C., Le Quéré, C., Myneni, R. B., Piao, S., and Thornton, P.: Carbon and other biogeochemical cycles. In: Climate Change 2013: The Physical

https://doi.org/10.5194/egusphere-2026-2606
Preprint. Discussion started: 29 July 2026

Science Basis. Cambridge Univ. Press, https://www.ipcc.ch/report/ar5/wg1/, 2014.

Thompson, R. L., Patra, P. K., Chevallier, F., Maksyutov, S., Law, R. M., Ziehn, T., van der Laan-Luijkx, I. T., Peters, W., Ganshin, A., Zhuravlev, R., Maki, T., Nakamura, T., Shirai, T., Ishizawa, M., Saeki, T., Machida, T., Poulter, B., Canadell, J. G., and Ciais, P.: Top-down assessment of the Asian carbon budget since the mid 1990s, Nat. Commun., 7, 10724, https://doi.org/10.1038/ncomms10724, 2016.

Morino, I., Matsuzaki, T., and Horikawa, M.: TCCON data from Tsukuba, Ibaraki, Japan, 125HR, Release GGG2014R2, Carbon Dioxide Information Analysis Center, Oak Ridge National Laboratory, https://doi.org/10.14291/tccon.ggg2014.tsukuba02.r2, 2018.

Fu, Y., Liao, H., Tian, X. J., Gao, H., Cai, Z. N., and Han, R.: Sensitivity of the simulated CO_2 concentration to inter-annual variations of its sources and sinks over East Asia, Adv. Clim. Change Res., 10, 250–263, https://doi.org/10.1016/j.accre.2020.03.001, 2019.

Xie, X., Huang, X., Wang, T., Li, M., Li, S., and Chen, P.: Simulation of non-homogeneous CO_2 and its impact on regional temperature in East Asia, J. Meteorol. Res., 32, 456–468, https://doi.org/10.1007/s13351-018-7123-x, 2018.

Yuan, Y., Sussmann, R., Rettinger, M., Ries, L., Petermeier, H., and Menzel, A.: Comparison of continuous in-situ CO_2 measurements with co-located column-averaged XCO_2 TCCON/satellite observations and CarbonTracker model over the Zugspitze region, Remote Sens., 11, 2981, https://doi.org/10.3390/rs11242981, 2019.

Cui, Y. Y., Jacobson, A. R., Feng, S., Barkley, Z. R., Davis, K. J., Zhang, L., Wesloh, D., Gerken, T., Keller, K., and Baker, D.: Evaluation of CarbonTracker's inverse estimates of North American net ecosystem exchange of CO_2 from different observing systems using ACT-America airborne observations, J. Geophys. Res.-Atmos., 126, e2020JD034406, https://doi.org/10.1029/2020JD034406, 2021.

She, W., Wu, Y., Huang, H., Chen, Z., Cui, G., Zheng, H., Guan, C., and Chen, F.: Integrative analysis of carbon structure and carbon sink function for major crop production in China's typical agriculture regions, J. Clean. Prod., 162, 702–708, https://doi.org/10.1016/j.jclepro.2017.05.108, 2017.

Li, J., Yu, Q., Sun, X., Tong, X., Ren, C., and Hu, Z.: Carbon dioxide exchange and the mechanism of environmental control in a farmland ecosystem in North China Plain, Sci. China Ser. D-Earth Sci., 49, Suppl. 2, 226–240, https://doi.org/10.1007/s11430-006-8226-1, 2006.

Han, D., Cai, H., Yang, X., and Xu, X.: Multi-source data modeling of the spatial distribution of winter wheat yield in China from 2000 to 2015, Sustainability, 12, 5436, https://doi.org/10.3390/su12135436, 2020.

Zhang, Y., Shen, Y., Liu, C., Yu, Q., Sun, H., Jia, J., Tang, C., and Kondoh, A.: Measurement of water, heat and CO_2 fluxes over a typical cropland in the North China Plain, Acta Geogr. Sin., 57, 335–344, https://doi.org/10.11821/xb200203010, 2002.

Lafleur, P. M., Roulet, N. T., and Admiral, S. W.: Annual cycle of CO_2 exchange at a bog peatland, J. Geophys. Res.-Atmos., 106, 3071–3081, https://doi.org/10.1029/2000jd900588, 2001.

Yue, Z., Li, Z., Yu, G., Chen, Z., Shi, P., Qiao, Y., Du, K., Tian, C., Zhao, F., Leng, P., Li, Z.,

https://doi.org/10.5194/egusphere-2026-2606
Preprint. Discussion started: 29 July 2026

Cheng, H., Chen, G., and Li, F.: Seasonal variations and driving mechanisms of CO_2 fluxes over a winter-wheat and summer-maize rotation cropland in the North China Plain, Agric. For. Meteorol., 342, 109699, https://doi.org/10.1016/j.agrformet.2023.109699, 2023.

Guo, J.-X., Li, Y.-Z., and Mei, X.-R.: Diurnal variation of instantaneous carbon dioxide flux and water use efficiency of wheat at field scale and analysis of influencing factors, Chin. J. Eco-Agric., 14, 78–81, 2006.

Dwyer, S. A., Ghannoum, O., Nicotra, A., and von Caemmerer, S.: High temperature acclimation of C4 photosynthesis is linked to changes in photosynthetic biochemistry, Plant Cell Environ., 30, 53–66, https://doi.org/10.1111/j.1365-3040.2006.01605.x, 2007.

Sage, R. F. and Kubien, D. S.: The temperature response of C3 and C4 photosynthesis, Plant Cell Environ., 30, 1086–1106, https://doi.org/10.1111/j.1365-3040.2007.01682.x, 2007

Wang, J., Wang, J., Zhao, H., and Zheng, Y.: Observation and simulation of CO_2 fluxes in rice paddy ecosystems based on the eddy covariance technique, Atmosphere, 15, 517, https://doi.org/10.3390/atmos15050517, 2024.

Song, L., Zhu, J., Li, M., Zhang, J., Zheng, X., and Wang, K.: Canopy transpiration of Pinus sylvestris var. mongolica in a sparse wood grassland in the semiarid sandy region of Northeast China, Agric. For. Meteorol., 250–251, 192–201, https://doi.org/10.1016/j.agrformet.2017.12.260, 2018.

Zhang, Q., Lei, H., Yang, D., Xiong, L., Liu, P., and Fang, B.: Decadal variation in CO_2 fluxes and its budget in a wheat and maize rotation cropland over the North China Plain, Biogeosciences, 17, 2245–2262, https://doi.org/10.5194/bg-17-2245-2020, 2020.

Yan, Y., Hou, P., Duan, F., Niu, L., Li, T., Zhang, S., Rui, X., Zhao, B., Xie, R., Ming, B., Wang, K., and Li, S.: Improving photosynthesis to increase grain yield potential: an analysis of maize hybrids released in different years in China, Photosynth. Res., 150, 295–311, https://doi.org/10.1007/s11120-021-00847-x, 2021.

Wang, W., Liao, Y. C., and Guo, Q.: Seasonal and annual variations of CO_2 fluxes in rain-fed winter wheat agro-ecosystem of Loess Plateau, China, J. Integr. Agr., 12, 147–158, https://doi.org/10.1016/S2095-3119(13)60215-4, 2013.

Demyan, M. S., Ingwersen, J., Funkuin, Y. N., Ali, R. S., Mirzaeitalarposhti, R., Rasche, F., Poll, C., Müller, T., Streck, T., Kandeler, E., and Cadisch, G.: Partitioning of ecosystem respiration in winter wheat and silage maize—modeling seasonal temperature effects, Agric. Ecosyst. Environ., 224, 131–144, https://doi.org/10.1016/j.agee.2016.03.039, 2016.

Zhang, Q., Lei, H.-M., and Yang, D.-W.: Seasonal variations in soil respiration, hetero trophic respiration and autotrophic respiration of a wheat and maize rotation cropl and in the North China Plain, Agric. Forest Meteorol., 180, 34–43, https://doi.org/10.1016/j.agrformet.2013.04.028, 2013.

Guo, H., Li, S., Wong, F. L., Qin, S. J., Wang, Y. H., Yang, D. N., and Lam, H. M.: Drivers of carbon flux in drip irrigation maize fields in northwest China, Carbon Balance Manage., 16, 12, https://doi.org/10.1186/s13021-021-00176-5, 2021.

Falge, E., Baldocchi, D., Tenhunen, J., Aubinet, M., Bakwin, P., Berbigier, P., Bernhofer, C., Burba, G., Clement, R., Davis, K. J., Elbers, J. A., Goldstein, A. H., Grelle, A., Granier, A., Guðmundsson, J., Hollinger, D., Kowalski, A. S., Katul, G., Law, B. E., Malhi, Y.,

https://doi.org/10.5194/egusphere-2026-2606
Preprint. Discussion started: 29 July 2026

Meyers, T., Monson, R. K., Munger, J. W., Oechel, W., Paw U, K. T., Pilegaard, K., Rannik, Ü., Rebmann, C., Suyker, A., Valentini, R., Wilson, K., and Wofsy, S.: Seasonality of ecosystem respiration and gross primary production as derived from FLUXNET measurements, Agric. Forest Meteorol., 113, 53–74, https://doi.org/10.1016/S0168-1923(02)00102-8, 2002.

Tao, F., Li, Y., Chen, Y., Yin, L., and Zhang, S.: Daily, seasonal and inter-annual variations in CO_2 fluxes and carbon budget in a winter-wheat and summer-maize rotation system in the North China Plain, Agric. Forest Meteorol., 324, 109098, https://doi.org/10.1016/j.agrformet.2022.109098, 2022.

Hollinger, S. E., Bernacchi, C. J., and Meyers, T. P.: Carbon budget of mature no-till ecosystem in North Central region of the United States, Agric. Forest Meteorol., 130, 59–69, https://doi.org/10.1016/j.agrformet.2005.01.005, 2005.

Wang, Y., Hu, C., Dong, W., Li, X., Zhang, Y., Qin, S., and Oenema, O.: Carbon budget of a winter-wheat and summer-maize rotation cropland in the North China Plain, Agric. Ecosyst. Environ., 206, 33–45, https://doi.org/10.1016/j.agee.2015.03.016, 2015.

Sun, X., Chang, Z., Yang, G., and Xu, X.: Characteristics of net ecosystem exchange and environmental factors of rice-wheat rotation system in the Yangtze River Delta of China, Chin. J. Eco-Agric., 23, 803–811, https://doi.org/10.13930/j.cnki.cjea.150007, 2015.

Zhang, K., Lu, Y., Duan, C., Zhang, F., Ling, X., Yao, Y., Wang, Z., Chen, X., Yan, S., Huo, Y., and Gong, Y.: Variations and drivers of CO_2 fluxes at multiple temporal scales of subtropical agricultural systems in the Huaihe river Basin, Agric. Forest Meteorol., 362, 110394, https://doi.org/10.1016/j.agrformet.2025.110394, 2025.

Lindner, S., Otieno, D., Lee, B., Xue, W., Arnhold, S., Kwon, H., Huwe, B., and Tenhunen, J.: Carbon dioxide exchange and its regulation in the main agro-ecosystems of Haean catchment in South Korea, Agric. Ecosyst. Environ., 199, 132–145, https://doi.org/10.1016/j.agee.2014.09.005, 2015.

Hu, X., Shi, L., Lin, L., Li, S., Deng, X., Li, J., Bian, J., Su, C., Du, S., Wang, T., Wang, Y., and Zhang, Z.: Accurate Estimation of Gross Primary Production of Paddy Rice Cropland with UAV Imagery-Driven Leaf Biochemical Model, Remote Sens., 16, 3906, https://doi.org/10.3390/rs16203906, 2024.

Schmidt, M., Reichenau, T. G., Fiener, P., and Schneider, K.: The carbon budget of a wheat field: an eddy covariance analysis of seasonal and inter-annual variability, Agric. Forest Meteorol., 165, 114–126, https://doi.org/10.1016/j.agrformet.2012.05.012, 2012.

Peng, X., Wang, Y., Ma, J., Liu, X., Gu, X., and Cai, H.: Seasonal variation and controlling factors of carbon balance over dry semi-humid cropland in Guanzhong Plain, Eur. J. Agron., 149, 126912, https://doi.org/10.1016/j.eja.2023.126912, 2023.

Lei, H. M. and Yang, D. W.: Seasonal and interannual variations in carbon dioxide exchange over a cropland in the North China Plain, Glob. Change Biol., 16, 2944–2957, https://doi.org/10.1111/j.1365-2486.2009.02136.x, 2010.

Chen, C., Li, D., Gao, Z., Tang, J., Guo, X., Wang, L., and Wan, B.: Seasonal and interannual variations of carbon exchange over a rice-wheat rotation system on the North China Plain, Adv. Atmos. Sci., 32, 1365–1380, https://doi.org/10.1007/s00376-015-4253-1, 2015.

https://doi.org/10.5194/egusphere-2026-2606
Preprint. Discussion started: 29 July 2026

Qader, S. H., Dash, J., and Atkinson, P. M.: Forecasting wheat and barley crop production in arid and semi-arid regions using remotely sensed primary productivity and crop phenology: a case study in Iraq, Sci. Total Environ., 613–614, 250–262, https://doi.org/10.1016/j.scitotenv.2017.09.057, 2018.

Wang, Y., Xu, X., Huang, L., Yang, G., Fan, L., Wei, P., and Chen, G.: An improved CASA model for estimating winter wheat yield from remote sensing images, Remote Sens., 11, 1088, https://doi.org/10.3390/rs11091088, 2019.

Lu, X., Zhang, X., Wang, Z., and Li, S.: Carbon budget of paddy ecosystems in China simulated by denitrification-decomposition model, Ecosphere, 15, e4926, https://doi.org/10.1002/ecs2.4926, 2024.

Weng, L., Zhu, Z., Han, X., and Tan, J.: Spatial-temporal pattern of net carbon sink of farmland vegetation in Jiangsu Province, Trans. Chin. Soc. Agric. Eng., 34, 233–241, https://doi.org/10.11975/j.issn.1002-6819.2018.06.030, 2018.

Wang, X., Wang, X., Wei, Q., Wang, W., Wang, S., Huo, Z., and Lei, H.: Coupling of net ecosystem CO_2 exchange and evapotranspiration of irrigated maize field in arid areas, J. Hydrol., 603, 127140, https://doi.org/10.1016/j.jhydrol.2021.127140, 2021.

Wang, X., Li, X., Tan, M., and Xin, L.: Remote sensing monitoring of changes in wheat area in North China Plain from 2001 to 2011, Trans. Chin. Soc. Agric. Eng., 31, 190–199, https://doi.org/10.3969/j.issn.1002-6819.2015.08.028, 2015.

Xin, L., Li, X., Tan, M., and Hao, H.: The rise of ordinary labor wage and its effect of agricultural land use in present China, Geogr. Res., 30, 1391–1400, https://doi.org/10.11821/yj2011080004, 2011.

Cai, J. and Tang, Z.: The development of agricultural mechanization in North China Plain and the formation of agricultural mechanization service market, Reform, 10, 65–72, https://doi.org/SUN:REFO.0.2016-10-010, 2016.

Long, H.: Land use policy in China: Introduction, Land Use Policy, 40, 1–5, https://doi.org/10.1016/j.landusepol.2014.03.006, 2014.

Zhang, J. R., Wang, Y. W., Zhang, M., Diao, Y. W., and Liu, C.: Optimization and validation of the vegetation photosynthesis and respiration model in a temperate broad-leaved Korean pine forest, Acta Ecol. Sin., 37, 6679–6690, https://doi.org/10.5846/stxb201607291552, 2017.

Liu, C., Huang, J.-P., Diao, Y.-W., Wen, X.-F., Xiao, W., Zhang, M., Lee, X.-H., and Liu, S.-D.: Optimization and evaluation of vegetation photosynthesis and respiration model using the measurements collected from the forest site of subtropical coniferous-evergreen, Chin. J. Plant Ecol., 39, 388–397, https://doi.org/10.17521/cjpe.2015.0038, 2015.

Diao, Y., Huang, J., Liu, C., Cui, J., and Liu, S.: A modeling study of CO_2 flux and concentrations over the Yangtze River Delta using the WRF-GHG model, Chin. J. Atmos. Sci., 39, 849–860, https://doi.org/10.3878/j.issn.1006-9895.1409.14127, 2015.

Gerbig, C. and Koch, F. T.: Biosphere-atmosphere exchange fluxes for CO_2 from the Vegetation Photosynthesis and Respiration Model VPRM for 2006–2022, https://doi.org/10.18160/VX78-HVA1, 2023.

https://doi.org/10.5194/egusphere-2026-2606
Preprint. Discussion started: 29 July 2026

Geels, C., Gloor, M., Ciais, P., Bousquet, P., Peylin, P., et al.: Comparing atmospheric transport models for future regional inversions over Europe – Part 1: Mapping the atmospheric CO_2 signals, Atmos. Chem. Phys., 7, 3461–3479, https://doi.org/10.5194/acp-7-3461-2007, 2007.

Mai, B., Diao, Y., Yang, H., Deng, T., Zou, Y., Wang, Y., Lan, W., Liu, X., and Deng, X.: Assessing atmospheric CO_2 concentrations and contributions from biogenic and anthropogenic sources in the Pearl River Delta region, Urban Clim., 54, 101864, https://doi.org/10.1016/j.uclim.2024.101864, 2024.

Ballav, S., Patra, P. K., Takigawa, M., Ghosh, S., De, U. K., Maksyutov, S., Murayama, S., Mukai, H., and Hashimoto, S.: Simulation of CO_2 concentration over East Asia using the regional transport model WRF-CO_2, J. Meteorol. Soc. Jpn., 90, 959–976, https://doi.org/10.2151/jmsj.2012-607, 2012.

Kim, H. M. and Kim, D.: Effect of boundary conditions on adjoint-based forecast sensitivity observation impact in a regional model, J. Atmos. Ocean. Technol., 38, 1233–1247, https://doi.org/10.1175/JTECH-D-20-0040.1, 2021.

Pillai, D., Gerbig, C., Ahmadov, R., Rödenbeck, C., Kretschmer, R., Koch, T., et al.: High-resolution simulations of atmospheric CO_2 over complex terrain – representing the Ochsenkopf mountain tall tower, Atmos. Chem. Phys., 11, 7445–7464, https://doi.org/10.5194/acp-11-7445-2011, 2011.